

Micromodulation: Induction of Intramolecular Electron Transfer by Solvate Molecule Dynamics in Mixed-Valence $[\text{Fe}_3\text{O}(\text{O}_2\text{CCH}_3)_6(3\text{-Me-py})_3](\text{solvate})$

Seung Mo Oh,¹ Scott R. Wilson,¹ David N. Hendrickson,^{*1} Scott E. Woehler,² Richard J. Wittebort,^{*2} Daryl Inniss,³ and Charles E. Strouse^{*3}

Contribution from the School of Chemical Sciences, University of Illinois, Urbana, Illinois 61801, the Department of Chemistry, University of Louisville, Louisville, Kentucky 40292, and the Department of Chemistry and Biochemistry, University of California, Los Angeles, California 90024. Received June 27, 1986

Abstract: The oxo-centered, trinuclear, mixed-valence iron acetate complexes $[\text{Fe}_3\text{O}(\text{O}_2\text{CCH}_3)_6(3\text{-Me-py})_3]\text{-S}$, where S = CH_3CN (**1**), toluene (**2**), 3-methylpyridine (**3**), and benzene (**4**), have been prepared, and the intramolecular electron transfer properties in the solid state have been studied. It is found that the rate of electron transfer is dramatically influenced by changing the solvate molecule. The complex **1** crystallizes in the monoclinic space group $P2_1/c$ with 4 molecules in a unit cell which has dimensions $a = 12.760$ (5) Å, $b = 26.233$ (11) Å, $c = 14.819$ (5) Å, and $\beta = 116.20$ (3)°. Compound **2** crystallizes in the triclinic space group $P\bar{1}$ with $Z = 2$, $a = 13.056$ (4) Å, $b = 15.902$ (3) Å, $c = 12.896$ (2) Å, $\alpha = 102.82$ (2)°, $\beta = 118.96$ (2)°, and $\gamma = 70.02$ (2)°. The complex **3**, isostructural with **2**, was characterized in the triclinic space group $A\bar{1}$ with $Z = 4$: at 128 K, $a = 12.964$ (5) Å, $b = 12.976$ (4) Å, $c = 29.293$ (9) Å, $\alpha = 84.01$ (1)°, $\beta = 94.41$ (1)°, and $\gamma = 121.76$ (1)°; at 298 K, $a = 13.114$ (4) Å, $b = 13.052$ (4) Å, $c = 30.054$ (5) Å, $\alpha = 85.81$ (4)°, $\beta = 95.23$ (4)°, and $\gamma = 120.99$ (5)°. The complex **1** has valence-trapped electronic states from 120 to 298 K on the Mössbauer time scale, and non-equivalent metal sites are seen in its single-crystal X-ray structure. The other three complexes are isostructural as indicated by the single-crystal X-ray structures of **2** and **3** and by a comparison of room-temperature powder X-ray diffraction patterns determined for all three complexes. The three complexes **2**, **3**, and **4** also exhibit similar Mössbauer spectra. At temperatures below ~ 100 K there are two doublets in the area ratio of two (high-spin Fe^{II}) to one (high-spin Fe^{III}). Increasing the sample temperature of **2**, **3**, and **4** above ~ 100 K leads to the appearance of a third average-valence doublet with a small spectral area. Eventually the spectrum changes upon increasing the temperature to become a single-average doublet. The X-ray structural work for **3** carried out at 298 and 128 K shows that the dimensions of the Fe_3O triangular complex change appreciably with temperature. The Fe_3 triangle of **3** at 128 K is asymmetric with three inequivalent Fe ions; the triangle becomes more equilateral at the higher temperature. The solid-state packing arrangement of **2**, **3**, and presumably **4** consists of Fe_3O units arranged two-dimensionally in layers with the solvate molecule located in an open space made by three neighboring Fe_3O molecules. In the case of **1** CH_3CN molecules are sandwiched between pairs of Fe_3O molecules. The Fe_3O complexes in **2** and **3** adopt a symmetric conformation with all three 3-methylpyridine ligands approximately perpendicular to the Fe_3O plane, while in **1** two of the 3-methylpyridine ligands are parallel to the Fe_3O plane. The effects of conformation on the charge distribution and intramolecular electron-transfer rate are discussed in light of these and previously reported results. Intramolecular electron transfer is slow in **1** because the environment about the Fe_3O complexes in **1** leads to an asymmetric complex with inequivalent iron ions. This inequivalence introduces appreciable potential-energy barriers for intramolecular electron transfer. In the case of **2**, **3**, and **4** it is suggested that an order-disorder phase transition involving motion of the solvate molecules influences the rate of intramolecular electron transfer. A single-crystal ^2H NMR study of **2** with perdeuterated toluene shows that at 293 K the toluene solvate molecules are involved in two motions. There is a twofold ring flip about the para axis, and the toluene solvate molecule is jumping between two lattice positions. Variable-temperature (290 to 140 K) ^2H NMR data are presented for a microcrystalline sample of **2** with perdeuterated toluene to show that, while the solvate molecule motion has not completely stopped by 140 K, the motion has slowed down considerably.

A variety of transition-metal complexes are known to change their structures and electronic states in the solid state as a result of a change in temperature. These compounds often exhibit interesting phase transition phenomena, in which the change in electronic state is strongly coupled with a change in the lattice.

Thermochromic complexes exhibit a color change as the temperature of the solid is varied, largely due to changes in coordination geometry and ligand field strength.⁴ Thermochromic complexes are frequently involved in structural phase transitions. One interesting class of compounds which show thermochromism has the composition $[\text{M}(\text{diäten})_2]\text{X}_2$, where diäten is *N,N*-diethylethylenediamine, M is Cu^{II} or Ni^{II} , and X is an anion.⁵⁻⁷ With anions such as halides and AgI_2^- which cannot become disordered in a thermodynamic sense, the color change occurs

continuously. On the other hand, with anions such as ClO_4^- , BF_4^- , and NO_3^- which can become orientationally disordered, the complexes change colors discontinuously as a result of a structural phase transition. It is believed that the phase transition involves either the onset of dynamic disorder of the diäten ligand and/or dynamic rotational disorder of the anion. The latter possibility is still under discussion.⁸

In addition to thermochromic compounds, several organic and inorganic salts with anions such as ClO_4^- show order-disorder phase transitions.⁹⁻¹³ In these salts, the phase transitions are believed to be triggered by a disordering in the orientation of the oxygen atoms of the anion. The anion goes from a static situation to a dynamic situation. For example, the conduction charac-

(8) Bloomquist, D. R.; Willett, R. D.; Dodgen, H. W. *J. Am. Chem. Soc.* **1981**, *103*, 2610.

(9) Nicolini, C.; Reiff, W. M. *Inorg. Chim. Acta* **1983**, *68*, 55.

(10) Knorr, K.; John, I. R.; Heger, G. *Solid State Commun.* **1974**, *15*, 231.

(11) Mody, J. H. M.; DeJong, H. J.; Glasbeek, M.; Van Voorst, J. D. W. *Chem. Phys. Lett.* **1973**, *18*, 51.

(12) Latoore, R.; Abeledo, C. R.; Frankel, R. B.; Costamagna, J. A.; Reiff, W. M.; Frank, E. *J. Chem. Phys.* **1973**, *59*, 2580.

(13) Reiff, W. M.; Long, G. J. In *Mössbauer Spectroscopy Applied to Inorganic Chemistry*; Long, G. J., Ed.; Plenum: New York, 1984.

(1) University of Illinois.

(2) University of Louisville.

(3) University of California.

(4) Bloomquist, D. R.; Willett, R. D. *Coord. Chem. Rev.* **1982**, *47*, 125.

(5) Grenthe, I.; Paoletti, P.; Sandstrom, M.; Glikberg, S. *Inorg. Chem.* **1979**, *18*, 2687.

(6) Yokoi, H.; Sai, M.; Isobe, T. *Bull. Chem. Soc. Jpn.* **1969**, *42*, 2232.

(7) Fabbri, L.; Micheloni, M.; Paoletti, P. *Inorg. Chem.* **1974**, *13*, 3019.

teristics of the quasi-one-dimensional superconductor (TMTSF)₂ClO₄, where TMTSF is tetramethyltetraselenafulvalene, have been shown to be dramatically influenced by the disorder in the ClO₄⁻ counterion.^{14,15}

Jahn-Teller distorted complexes comprise another class of electronically labile molecules that are known to be involved in structural phase transitions.¹⁶⁻²⁴ Ammeter, Bürgi, and co-workers²² carefully studied [Cu(tach)₂](NO₃)₂, where tach is *cis,cis*-1,3,5-triaminocyclohexane. This nitrate salt undergoes a phase transition at ~120 K, where below 120 K Cu(tach)₂²⁺ is statically distorted, and immediately above 150 K it dynamically oscillates between two and, at higher temperatures, between all three possible tetragonal elongations of the CuN₆ octahedron. The phase transition at 120 K is sudden. There are hydrogen bonding interactions between NO₃⁻ and Cu(tach)₂²⁺ that are probably important in the phase transition.

Order-disorder phase transitions involving the solvate molecule have also been noted for spin-crossover complexes.²⁵⁻²⁷ For example, the conversion from high spin to low spin is abrupt for [Fe(2-pic)₃]Cl₂-solvate, where 2-pic is 2-picolyamine.^{25b,28} Hysteresis is exhibited by the ethanol, methanol, and water solvates. The existence of a two-dimensional hydrogen-bonding network was revealed in the X-ray structures²⁹ of the ethanol and methanol solvates. Deuteration of the OH proton of the ethanol and methanol solvate molecules has been shown to have an appreciable effect on the critical temperature of the spin-crossover phase transition.^{28d,30} An order-disorder transition of the ethanol solvate molecules was also found in the structural work. Non-linearity of a plot of ln *K* vs. 1/*T* for the spin transition has been attributed to a coupling between the spin-state interconversion and this transition. Recently heat-capacity measurements³¹ have been carried out on microcrystalline [Fe(2-pic)₃]Cl₂·C₂H₅OH. Two phase transitions at 114 and 122 K were observed. The microscopic nature of these two phase transitions is not known; however, the experimental value for the total entropy change for both phase transitions can be accounted for by a combination of a magnetic transition, the orientational order-disorder conversion of the solvate molecules, and a change in the phonon system, in particular a change in metal-ligand vibrations.

In a recent communication^{32a} we showed that a change in the solvate molecule dramatically affects the rate of intramolecular electron transfer in mixed-valence [Fe₃O(O₂CCH₃)₆(L)₃]·S. In these complexes L is pyridine or a substituted pyridine and the solvate molecule S can be molecules such as benzene, chloroform, acetonitrile, or a pyridine. It was suggested that the onset of dynamic disorder of the ligands L and/or solvate molecules dramatically affected the rate of electron transfer in the Fe₃O complexes.³³ The presence of two phase transitions (~112 and ~190 K) was detected by heat-capacity measurements for [Fe₃O(O₂CCH₃)₆(py)₃](py), where py is pyridine.³³ In this same recent communication³³ it was also shown with ⁵⁷Fe Mössbauer data that the temperature of these two phase transitions corresponds to the onset of intramolecular electron transfer at ~112 K and the occurrence at ~190 K of a rate of electron transfer that exceeds the ⁵⁷Fe Mössbauer time scale. Single-crystal solid-state ²H NMR data were also presented^{33a,34} for an analogous iron-acetate complex to show that the benzene solvate molecules are rotating rapidly from 300 to 150 K about a crystallographic C₃ axis, the axis along which the Fe₃O complexes are stacked (i.e., the benzene molecules are perpendicular to and sandwiched between two Fe₃O complexes).

In the present manuscript results are presented for the series [Fe₃O(O₂CCH₃)₆(3-Me-py)₃]·S, where 3-Me-py is 3-methylpyridine and S is 3-Me-py, CH₃CN, benzene, or toluene. Single-crystal X-ray structural results are presented for three of the complexes, one that does not show the onset of electron transfer with increasing temperature and two that do. It was of interest to see what differences in packing arrangements lead to these two different electron-transfer characteristics. Since the 3-Me-py solvate does exhibit an increasing rate of electron transfer with increasing temperature, the X-ray structure of this complex was determined at 128 and 298 K. Finally solid-state ²H NMR spectra were run for two complexes prepared with deuterated solvate molecules to determine whether in fact there is an onset of solvate molecule dynamics that is controlling the rate of intramolecular electron transfer in the Fe₃O complexes.

Experimental Section

Physical Measurements. Variable-temperature ⁵⁷Fe Mössbauer spectra were obtained in vertical transmission geometry with use of a constant acceleration spectrometer that has been described before.³⁵ The source originally consisted of 50 mCi of ⁵⁷Co diffused into a 12-μm rhodium matrix. Temperature control was carried out by means of a Lake Shore Cryotronics Model DTC-500-SP temperature controller. Sample temperature measurements are made with a calibrated Allen Bradley 560 Ω, 1/8 W carbon resistor mounted in the copper sample cell holder. The estimated accuracy of absolute sample temperature determination is ±1 K below 10 K, better than ±2 K for the 10–30 K region, and ±3 K for temperatures above ~30 K. The relative precision of temperature determination is ±0.5 K at the higher temperatures. Isomer shift data are reported relative to iron foil at 298 K but are not corrected for temperature-dependent second-order Doppler effects. It should be noted that isomer shifts illustrated in the figures are displaced slightly from the actual values, whereas accurate isomer shift values are to be found in the tabulated results. Computer fittings of the Mössbauer data to Lorentzian line shapes were carried out with a modified version of a previously reported computer program.³⁶

²H NMR experiments were performed on a homebuilt 5.9-T spectrometer described elsewhere.³⁷ The pulse sequence used was [(90)_x-

(14) Beno, M. A.; Blackman, G. S.; Leung, P. C. W.; Williams, J. M. *Solid State Commun.* **1983**, *48*, 99.

(15) Pouget, J. P.; Shirane, G.; Beckgaard, K. *Phys. Rev.* **1983**, *B27*, 5203.

(16) (a) Bersuker, I. B. *Coord. Chem. Rev.* **1975**, *14*, 357. (b) Bersuker, I. B. *The Jahn-Teller Effect and Vibronic Interactions in Modern Chemistry*; Plenum: New York, 1984.

(17) Gehring, G. A.; Gehring, K. A. *Rep. Prog. Phys.* **1975**, *38*, 1.

(18) Reinen, D.; Friebel, C. *Struct. Bonding (Berlin)* **1979**, *37*, 1.

(19) Gazo, J.; Bersuker, I. B.; Gara, J.; Kabesova, M.; Kohout, J.; Langfelderova, H.; Melnik, M.; Serator, M.; Valach, F. *Coord. Chem. Rev.* **1976**, *19*, 253.

(20) Hathaway, B.; Duggan, M.; Murphy, A.; Mullane, J.; Power, C.; Walsh, A.; Walsh, B. *Coord. Chem. Rev.* **1981**, *36*, 267.

(21) Hathaway, B. *Coord. Chem. Rev.* **1982**, *41*, 423.

(22) Ammeter, J. H.; Bürgi, H. B.; Gamp, E.; Meyer-Sandrin, V.; Jensen, W. P. *Inorg. Chem.* **1979**, *18*, 733.

(23) Simmons, C. J.; Clearfield, A.; Fitzgerald, W.; Tyagi, S.; Hathaway, B. J. *Inorg. Chem.* **1983**, *22*, 2463.

(24) Sturge, M. D. *Solid State Phys.* **1967**, *20*, 91.

(25) (a) Gütllich, P. *Struct. Bonding (Berlin)* **1981**, *44*, 83. (b) Gütllich, P. In *Chemical Mössbauer Spectroscopy*; Herber, R. H., Ed.; Plenum: New York, 1984.

(26) Rao, C. N. R. *Int. Rev. Phys. Chem.* **1985**, *4*, 19.

(27) König, E.; Ritter, G.; Kulshreshtha, S. K. *Chem. Rev.* **1985**, *85*, 219.

(28) (a) Renovitch, G. A.; Baker, W. A., Jr. *J. Am. Chem. Soc.* **1967**, *89*, 6377. (b) Sorai, M.; Enslin, J.; Gütllich, P. *Chem. Phys.* **1976**, *18*, 199. (c) Sorai, M.; Enslin, J.; Hasselbach, K. M.; Gütllich, P. *Chem. Phys.* **1977**, *20*, 197. (d) Gütllich, P.; Köppen, H.; Steinhäuser, H. G. *Chem. Phys. Lett.* **1980**, *74*, 475.

(29) (a) Greenway, A. M.; O'Connor, C. J.; Schrock, A.; Sinn, E. *Inorg. Chem.* **1979**, *18*, 2692. (b) Katz, B. A.; Strouse, C. E. *J. Am. Chem. Soc.* **1979**, *101*, 6214. (c) Mikami, M.; Konno, M.; Saito, Y. *Chem. Phys. Lett.* **1979**, *63*, 566. (d) Mikami-Kido, M.; Saito, Y. *Acta Crystallogr.* **1982**, *B38*, 452.

(30) See pages 46–49 of ref 25b.

(31) Kaji, K.; Sorai, M. *Thermochim. Acta*, in press.

(32) (a) Oh, S. M.; Hendrickson, D. N.; Hassett, K. L.; Davis, R. E. *J. Am. Chem. Soc.* **1984**, *106*, 7984. (b) Oh, S. M.; Hendrickson, D. N.; Hassett, K. L.; Davis, R. E. *J. Am. Chem. Soc.* **1985**, *107*, 8009–8018.

(33) (a) Oh, S. M.; Kambara, T.; Hendrickson, D. N.; Sorai, M.; Kaji, K.; Woehler, S. E.; Wittebort, R. J. *J. Am. Chem. Soc.* **1985**, *107*, 5540. (b) Full paper detailing heat capacity data: Sorai, M.; Kaji, K.; Hendrickson, D. N.; Oh, S. M. *J. Am. Chem. Soc.* **1986**, *108*, 702–708.

(34) Woehler, S. E.; Wittebort, R. J.; Oh, S. M.; Hendrickson, D. N.; Inniss, D.; Strouse, C. E. *J. Am. Chem. Soc.* **1986**, *108*, 2938.

(35) Cohn, M. J.; Timken, M. D.; Hendrickson, D. N. *J. Am. Chem. Soc.* **1984**, *106*, 6683.

(36) Münck, E.; Groves, J. L.; Tumolillo, T. A.; Debrunner, P. G. *Comput. Phys. Commun.* **1973**, *5*, 225.

(37) (a) Wittebort, R. J.; Subramanian, R.; Kulshreshtha, N. P.; DuPre, D. B. *J. Chem. Phys.* **1985**, *83*, 2457. (b) Woehler, S. E.; Wittebort, R. J. *J. Magn. Reson.*, submitted for publication.

$1/2-(180)_y-1/2-(90)_y-1/2-(180)_y-1/2$ -observe], which refocuses both the quadrupolar and paramagnetic couplings.³⁸ In this sequence a value of $t = 35 \mu\text{s}$ was used. This requires a probe-receiver recovery time of less than $18 \mu\text{s}$.

NMR samples were ~ 50 mg of tightly or loosely packed microcrystalline material sealed into a Delrin tube ($1/4$ in. \times $1/2$ in.). In the case of the single-crystal work, a crystal approximately $1 \text{ mm} \times 1 \text{ mm} \times 1 \text{ mm}$ was placed into a 0.176-in. cube with a 0.114-in. hole drilled into one face and subsequently filled with degassed eicosane. The crystal could then be rotated about axes normal to three cube faces and perpendicular to H_0 . For the magnetically oriented single-crystal work, the cube containing the crystal fixed in position with eicosane was placed in the magnetic field with the normal of the drilled face parallel to the field. A stream of dry nitrogen gas at 50°C was passed over the cube, melting the eicosane and allowing the crystal to orient. Subsequently, spectra were obtained at temperatures below the melting point of eicosane (46°C).

The signal-to-noise ratio varied with crystal orientation with spectra from z -axis rotation giving the best results. To obtain reliable spectra it took from 2000 to 15000 transients with a delay of 250 ms between transients.

Compound Preparation. 3-Methylpyridine (3-Me-py) was dried by refluxing with BaO and then fractionally distilled under vacuum. Acetonitrile was dried over P_2O_5 and distilled under an argon atmosphere. All elemental analyses were performed in the Microanalytical Laboratory of the School of Chemical Sciences, University of Illinois. Due to the sensitivity to air and water of the compounds in solution and to a lesser degree in the solid state, reactions were carried out under an argon atmosphere in either Schlenk vessels or an inert-atmosphere glovebox (Vacuum Atmospheres Corp.).

$[\text{Fe}_3\text{O}(\text{O}_2\text{CCH}_3)_6(\text{H}_2\text{O})_3]$. This mixed-valence compound was prepared by a previously reported method.³⁹ $\text{FeCl}_2 \cdot 4\text{H}_2\text{O}$ (20 g, 0.1 mol), sodium acetate (20 g, 0.24 mol), and glacial acetic acid (60 g, 1 mol) were dissolved in 100 mL of water. The reaction mixture was heated at $70\text{--}80^\circ\text{C}$ under reflux for 2 h, while bubbling a constant stream of air. The mixture was cooled to room temperature and the dark-brown precipitate was filtered, washed with ethanol and ethyl ether, and then dried under vacuum. The yield was 10.4 g (52.7%).

$[\text{Fe}_3\text{O}(\text{O}_2\text{CCH}_3)_6(3\text{-Me-py})_3](3\text{-Me-py})$. Samples of this compound were prepared by the method given by Lupu and Ripan⁴⁰ for the preparation of $[\text{Fe}_3\text{O}(\text{O}_2\text{CCH}_3)_6(\text{py})_3](\text{py})$. $[\text{Fe}_3\text{O}(\text{O}_2\text{CCH}_3)_6(\text{H}_2\text{O})_3]$ (5 g, 8.4 mmol) was dissolved in 30 mL of 3-methylpyridine under argon atmosphere. The reaction mixture was stirred for 1 h at $50\text{--}60^\circ\text{C}$, and then it was slowly evaporated for 3 days. The black crystalline product was filtered off and dried under vacuum. Crystals suitable for X-ray crystallography were grown by slow evaporation of a 3-methylpyridine solution under an argon atmosphere. Anal. Calcd for $\text{C}_{36}\text{Fe}_3\text{H}_{46}\text{N}_4\text{O}_{13}$: C, 47.50; Fe, 18.41; H, 5.09; N, 6.15. Found: C, 47.33; Fe, 18.35; H, 5.03; N, 6.02.

$[\text{Fe}_3\text{O}(\text{O}_2\text{CCH}_3)_6(3\text{-Me-py})_3](\text{CH}_3\text{CN})$, $[\text{Fe}_3\text{O}(\text{O}_2\text{CCH}_3)_6(3\text{-Me-py})_3](\text{toluene})$, and $[\text{Fe}_3\text{O}(\text{O}_2\text{CCH}_3)_6(3\text{-Me-py})_3](\text{benzene})$ were prepared by recrystallizing $[\text{Fe}_3\text{O}(\text{O}_2\text{CCH}_3)_6(3\text{-Me-py})_3](3\text{-Me-py})$ in CH_3CN , toluene, or benzene, respectively. X-ray quality crystals of the first two complexes were grown by slow evaporation. Anal. Calcd for $[\text{Fe}_3\text{O}(\text{O}_2\text{CCH}_3)_6(3\text{-Me-py})_3](\text{CH}_3\text{CN})$: C, 44.78; Fe, 19.52; H, 4.93; N, 6.52. Found: C, 44.56; Fe, 19.11; H, 4.94; N, 6.61. Anal. Calcd for $[\text{Fe}_3\text{O}(\text{O}_2\text{CCH}_3)_6(3\text{-Me-py})_3](\text{toluene})$: C, 48.87; Fe, 18.43; H, 5.21; N, 4.62. Found: C, 49.10; Fe, 18.31; H, 5.24; N, 4.66. Anal. Calcd for $[\text{Fe}_3\text{O}(\text{O}_2\text{CCH}_3)_6(3\text{-Me-py})_3](\text{benzene})$: C, 48.30; Fe, 18.71; H, 5.07; N, 4.69. Found: C, 48.26; Fe, 18.96; H, 5.05; N, 4.56.

Crystal Measurements, Data Collection, and Structure Refinement for $[\text{Fe}_3\text{O}(\text{O}_2\text{CCH}_3)_6(3\text{-Me-py})_3](3\text{-Me-py})$. A dark blue crystal ($0.24 \times 0.36 \times 0.43 \text{ mm}$) was used for data collection at the University of California. The 128 K and 298 K data sets were collected with a locally automated Picker diffractometer equipped with a gas-stream low-temperature device. The crystal was mounted on a glass fiber. The unit cell parameters were obtained by a least-squares fit to the automatically centered settings of 12 reflections. The same crystal was used to collect both data sets. Experimental parameters associated with the data collection can be found in Table I. Three reflections monitored after every 97 reflections showed no significant variation in intensity. Intensities were derived from an analysis of the scan profiles.⁴¹ The data were

Table I. Crystallographic Data for $[\text{Fe}_3\text{O}(\text{O}_2\text{CCH}_3)_6(3\text{-Me-py})_3](3\text{-Me-py})$ at 128 and 298 K

T, K	128 K	298 K
crystal system	triclinic	triclinic
cryst dimens, mm	$0.24 \times 0.36 \times 0.43$	same as 128 K
space group	$A\bar{1}$	$A\bar{1}$
Z	4	4
a, Å	12.964 (5)	13.114 (4)
b, Å	12.976 (4)	13.054 (5)
c, Å	29.293 (9)	30.054 (5)
α , deg	84.01 (1)	85.81 (4)
β , deg	94.41 (1)	95.23 (4)
γ , deg	121.76 (1)	120.99 (5)
volume, Å ³	4165	4389
density (calcd), g/cm ³	1.45	1.38
radiation, Å	Mo, 0.7107	Mo, 0.7107
scan rate, deg/min	6	6
scan mode	θ - 2θ	θ - 2θ
2θ max, deg	50	45
reflens ($I > 3\sigma I$)	6198	3404
R	0.047	0.063
R_w	0.071	0.084
EOF	2.67	2.75
no. of parameters refined	476	346

corrected for Lorentz and polarization effects. Transmission factors varied between 0.77 and 0.59; no absorption correction was applied.

Direct methods (MULTAN) were used to solve the structure in the space group $A\bar{1}$. The unconventional cell was chosen because of the pseudo-hexagonal lattice parameters. The unique non-hydrogen atoms were located by successive cycles of full-matrix least-squares refinement and difference Fourier synthesis. The disordered solvate molecule was modeled by two rigid groups (C-C = 1.39 Å, C-H = 1.00 Å, C-C(methyl) = 1.50 Å). The position and orientation of each group were refined. A single isotropic group temperature factor was refined and assigned to both groups. The total occupancy of the two groups was constrained to equal 1. The disordered ligands were modeled by assignment of peaks found in the electron density difference map as methyl carbons at the 3 and 5 positions of the pyridine ring. Positions and anisotropic thermal parameters of these methyl carbon atoms were refined independently, and the total methyl occupancy of each ligand was constrained to equal 1.

Hydrogen atoms were included as fixed contributors to the final refinement cycles. At least one hydrogen atom for each methyl group was found in an electron density map. The other methyl hydrogen atoms were calculated on the basis of idealized geometry (sp^3) and bond length (C-H = 1.00 Å). Some of the hydrogen atoms on the pyridine rings were idealized (sp^2) with C-H = 1.00 Å. All nonsolvate hydrogen atoms were assigned isotropic temperature factors of $B = 4.00 \text{ \AA}^2$ at 298 K.

At 128 K, in the final cycles of least-squares refinement, all non-hydrogen and non-solvate atoms were refined with anisotropic thermal coefficients. The refinement converged at $R = 0.047$ and $R_w = 0.063$. The largest features in the final difference map were peaks at 1.77, 1.69, and 1.52 e/\AA^3 located near the iron atoms.

At 298 K the structure was similarly refined. All the carbon atoms in the pyridine ligands were refined isotropically as were some of the carbon atoms in the acetate. The refinement converged at $R = 0.071$ and $R_w = 0.084$. The largest features in the final difference map were peaks of 1.27, 1.17, and 1.11 e/\AA^3 located near the iron atoms.

The final positional parameters for all atoms can be found in Table II. Listings of the thermal parameters and observed and calculated structure factors are available in the supplementary material.

Crystal Measurements, Data Collection, and Structure Solution and Refinement for $[\text{Fe}_3\text{O}(\text{O}_2\text{CCH}_3)_6(3\text{-Me-py})_3](\text{toluene})$. The opaque dark blue prismatic crystal used for data collection had well-defined faces and edges. This crystal was one from a series determined to be quite pressure

(38) Siminovich, D. J.; Rause, M.; Jeffries, K. R.; Brown, M. F. *J. Magn. Reson.* **1984**, *58*, 62.

(39) Johnson, M. K.; Cannon, R. D.; Powell, D. B. *Spectrochim. Acta* **1982**, *38A*, 307.

(40) Lupu, D.; Ripan, R. *Rev. Roum. Chim.* **1971**, *16*, 43.

(41) The programs used in this work included modified versions of the following programs: CARESS (Broach, Coppens, Becker, and Blessing), peak profile analysis, Lorentz and polarization corrections; MULTAN (Main), package of programs, including direct methods, structure factor normalization, Fourier transform, and peak search; ORFLS (Busing, Martin, and Levy), structure factor calculation and full-matrix least-squares refinement; ORFFE (Busing, Martin, and Levy), distance, angle, and error calculations; ABSORB (Coppens, Edwards, and Hamilton), absorption correction calculation; ORTEP (Johnson) figure plotting; HYDROGEN (Trueblood), calculation of hydrogen atomic positions. All calculations were performed on a DEC VAX 11/750 crystallographic computer. Scattering factors and corrections for anomalous dispersion were taken from the following: *International Tables for X-ray Crystallography*; Kynoch: Birmingham, England, 1974; Vol. 4.

Table II. Positional Parameters for $[\text{Fe}_3\text{O}(\text{O}_2\text{CCH}_3)_6(3\text{-Me-py})_3](3\text{-Me-py})$ at 128 K

atom	<i>x/a</i>	<i>y/b</i>	<i>z/c</i>
Fe(01)	0.2042 (0)	0.0533 (0)	0.3791 (0)
Fe(02)	-0.0841 (0)	-0.1512 (0)	0.3662 (0)
Fe(03)	0.0029 (0)	0.1380 (0)	0.3562 (0)
O(1)	0.0396 (2)	0.0107 (2)	0.3668 (1)
O(2)	0.1969 (2)	-0.0651 (2)	0.3358 (1)
O(3)	0.009 (2)	-0.2089 (2)	0.3285 (1)
O(4)	0.1641 (2)	-0.0732 (2)	0.4351 (1)
O(5)	-0.0323 (2)	-0.2127 (2)	0.4249 (1)
O(6)	-0.1652 (2)	-0.1334 (2)	0.3065 (1)
O(7)	-0.1164 (2)	0.0601 (2)	0.3009 (1)
O(8)	-0.1992 (2)	-0.1375 (2)	0.4047 (1)
O(9)	-0.1409 (2)	0.0590 (2)	0.4007 (1)
O(10)	0.1099 (2)	0.2342 (2)	0.4107 (1)
O(11)	0.2459 (2)	0.1783 (3)	0.4255 (1)
O(12)	0.1407 (2)	0.2403 (2)	0.3101 (1)
O(13)	0.2783 (2)	0.1868 (2)	0.3262 (1)
N(20)	0.3942 (3)	0.0970 (3)	0.3926 (1)
N(30)	-0.2379 (3)	-0.3444 (3)	0.3663 (1)
N(40)	-0.0356 (3)	0.2860 (3)	0.3430 (1)
C(1)	0.1116 (3)	-0.1616 (3)	0.3208 (1)
C(2)	0.1444 (4)	-0.2298 (4)	0.2920 (1)
C(3)	0.0672 (3)	-0.1672 (3)	0.4472 (1)
C(4)	0.0658 (4)	-0.2337 (4)	0.4930 (2)
C(5)	-0.1698 (3)	-0.0447 (4)	0.2876 (1)
C(6)	-0.2469 (5)	-0.0678 (5)	0.2439 (2)
C(7)	-0.2056 (3)	-0.0497 (3)	0.4163 (1)
C(8)	-0.2958 (4)	-0.0786 (4)	0.4519 (2)
C(9)	0.1946 (3)	0.2335 (3)	0.4341 (1)
C(10)	0.2375 (4)	0.3032 (5)	0.4769 (2)
C(11)	0.2384 (3)	0.2464 (3)	0.3030 (1)
C(12)	0.3149 (4)	0.3331 (4)	0.2646 (2)
C(21)	0.4431 (4)	0.1191 (4)	0.4348 (2)
C(22)	0.5614 (4)	0.1498 (4)	0.4460 (2)
C(23)	0.6310 (4)	0.1577 (4)	0.4123 (2)
C(24)	0.5824 (4)	0.1356 (4)	0.3678 (2)
C(25)	0.4641 (4)	0.1052 (4)	0.3601 (2)
C(26)	0.6078 (5)	0.1697 (8)	0.4929 (2)
C(27)	0.6338 (18)	0.1100 (24)	0.3402 (7)
C(31)	-0.2688 (4)	-0.4044 (3)	0.3282 (1)
C(32)	-0.3648 (4)	-0.5229 (4)	0.3256 (2)
C(33)	-0.4337 (4)	-0.5807 (4)	0.3641 (2)
C(34)	-0.4015 (4)	-0.5213 (4)	0.4042 (2)
C(35)	-0.3024 (4)	-0.4030 (3)	0.4038 (1)
C(36)	-0.3800 (6)	-0.5872 (7)	0.2819 (3)
C(37)	-0.4519 (14)	-0.5746 (12)	0.4508 (6)
C(41)	-0.0520 (3)	0.3344 (3)	0.3776 (1)
C(42)	-0.0773 (3)	0.4266 (3)	0.3720 (1)
C(43)	-0.0819 (4)	0.4709 (3)	0.3275 (2)
C(44)	-0.0652 (4)	0.4226 (4)	0.2911 (1)
C(45)	-0.0433 (4)	0.3292 (4)	0.3001 (1)
C(46)	-0.0979 (5)	0.4745 (5)	0.4124 (2)
N(70)	0.6111	0.4317	0.6399
C(71)	0.7045	0.4395	0.6190
C(72)	0.6945	0.3290	0.6127
C(73)	0.5919	0.2192	0.6278
C(74)	0.4993	0.2198	0.6492
C(75)	0.5093	0.3302	0.6555
C(76)	0.7937	0.3284	0.5898
N(80)	0.6776	0.4455	0.6124
C(81)	0.5831	0.3566	0.6369
C(82)	0.5658	0.2403	0.6382
C(83)	0.6442	0.2218	0.6148
C(84)	0.7399	0.3195	0.5902
C(85)	0.7573	0.4357	0.5889
C(86)	0.4632	0.1356	0.6646

sensitive, making the samples difficult to mount in capillaries without damage. The sample was bound by the following forms: $\{001\}$, $\{010\}$, $\{10-1\}$, and $\{100\}$. The interfacial separations between inversion related faces were 0.38, 0.50, 0.50, and 0.62 mm, respectively. The crystal was mounted with use of a light film of grease in a sealed 0.7-mm thin-walled tapered glass capillary with the $(10-1)$ scattering planes roughly normal to the spindle axis.

Data collection at the University of Illinois was carried out at 298 K on a Enraf-Nonius CAD4 automated K-axis diffractometer. There was no evidence of twinning, and the mosaic spread was within acceptable

Table III. Positional Parameters for $[\text{Fe}_3\text{O}(\text{O}_2\text{CCH}_3)_6(3\text{-Me-py})_3](3\text{-Me-py})$ at 298 K

atom	<i>x/a</i>	<i>y/b</i>	<i>z/c</i>
Fe(01)	0.1966 (1)	0.0422 (1)	0.3844 (0)
Fe(02)	-0.0863 (1)	-0.1599 (1)	0.3677 (0)
Fe(03)	-0.0009 (1)	0.1264 (1)	0.3600 (0)
O(01)	0.0373 (4)	0.0027 (4)	0.3708 (2)
O(02)	0.1906 (5)	-0.0738 (5)	0.3411 (2)
O(03)	-0.0021 (5)	-0.2167 (4)	0.3298 (2)
O(04)	0.1612 (5)	-0.0793 (5)	0.4371 (2)
O(05)	-0.0308 (5)	-0.2171 (4)	0.4250 (2)
O(06)	-0.1697 (5)	-0.1416 (5)	0.3099 (2)
O(07)	-0.1185 (5)	0.0517 (5)	0.3055 (2)
O(08)	-0.1960 (5)	-0.1406 (4)	0.4059 (2)
O(09)	-0.1407 (5)	0.0531 (4)	0.4017 (2)
O(10)	0.1081 (5)	0.2267 (4)	0.4133 (2)
O(11)	0.2380 (5)	0.1678 (5)	0.4302 (2)
O(12)	0.1326 (6)	0.2226 (5)	0.3162 (2)
O(13)	0.2696 (5)	0.1734 (5)	0.3358 (2)
N(20)	0.3870 (6)	0.0854 (5)	0.3991 (2)
N(30)	-0.2364 (6)	-0.3506 (6)	0.3650 (2)
N(40)	-0.0357 (6)	0.2771 (5)	0.3474 (2)
C(01)	0.1036 (9)	-0.1680 (7)	0.3228 (3)
C(02)	0.1421 (9)	-0.2289 (8)	0.2915 (3)
C(03)	0.0650 (9)	-0.1724 (8)	0.4471 (3)
C(04)	0.0718 (9)	-0.2339 (9)	0.4900 (3)
C(05)	-0.1750 (8)	-0.0549 (9)	0.2917 (3)
C(06)	-0.2546 (10)	-0.0785 (9)	0.2502 (3)
C(07)	-0.2010 (8)	-0.0532 (8)	0.4172 (3)
C(08)	-0.2867 (9)	-0.0767 (8)	0.4513 (3)
C(09)	0.1900 (9)	0.2261 (8)	0.4372 (3)
C(10)	0.2344 (9)	0.3014 (8)	0.4778 (3)
C(11)	0.2297 (10)	0.2291 (8)	0.3114 (3)
C(12)	0.3032 (9)	0.3097 (9)	0.2755 (3)
C(21)	0.4356 (10)	0.1085 (9)	0.4397 (3)
C(22)	0.5561 (10)	0.1394 (9)	0.4506 (4)
C(23)	0.6182 (9)	0.1439 (8)	0.4167 (3)
C(24)	0.5710 (9)	0.1198 (8)	0.3745 (3)
C(25)	0.4510 (9)	0.0918 (7)	0.3662 (3)
C(26)	0.6027 (68)	0.1706 (65)	0.4935 (26)
C(27)	0.6350 (14)	0.1209 (13)	0.3359 (5)
C(31)	-0.2676 (8)	-0.4098 (8)	0.3274 (3)
C(32)	-0.3629 (9)	-0.5284 (8)	0.3246 (3)
C(33)	-0.4229 (9)	-0.5796 (8)	0.3608 (3)
C(34)	-0.3943 (9)	-0.5233 (8)	0.4005 (3)
C(35)	-0.2984 (8)	-0.4068 (8)	0.4011 (3)
C(36)	-0.3720 (26)	-0.5914 (27)	0.2822 (10)
C(37)	-0.4529 (22)	-0.5720 (21)	0.4428 (8)
C(41)	-0.0541 (7)	0.3240 (7)	0.3814 (3)
C(42)	-0.0727 (8)	0.4218 (8)	0.3754 (3)
C(43)	-0.0702 (9)	0.4665 (8)	0.3336 (3)
C(44)	-0.0551 (9)	0.4185 (8)	0.2983 (3)
C(45)	-0.0354 (8)	0.3223 (8)	0.3064 (3)
C(46)	-0.0937 (11)	0.4686 (10)	0.4153 (4)
N(70)	0.6091	0.4315	0.6412
C(71)	0.7008	0.4420	0.6202
C(72)	0.6962	0.3351	0.6126
C(73)	0.6002	0.2257	0.6267
C(74)	0.5089	0.2233	0.6483
C(75)	0.5135	0.3302	0.6558
C(76)	0.7941	0.3377	0.5894
N(80)	0.7096	0.4371	0.5840
C(81)	0.6259	0.3974	0.6141
C(82)	0.5734	0.2765	0.6272
C(83)	0.6084	0.2043	0.6091
C(84)	0.6960	0.2531	0.5780
C(85)	0.7486	0.3741	0.5649
C(86)	0.4795	0.2241	0.6606

limits. The unit cell parameters, listed in Table III, were obtained by a least-squares fit to the automatically centered settings for 25 reflections. Details of the data collection may also be found in Table IV. No change in the appearance of the sample was noted during the experiment. Corrections to the data were made for Lorentz and polarization effects and for anomalous dispersion effects. A numerical correction for absorption was applied, and the maximum and minimum transmission factors were 0.721 and 0.618.

Since this toluene solvate crystal was found to be isomorphous to $[\text{Fe}_3\text{O}(\text{O}_2\text{CCH}_3)_6(3\text{-Me-py})_3](3\text{-Me-py})$, positions for all atoms (except

Table IV. Crystallographic Parameters for $[\text{Fe}_3\text{O}(\text{O}_2\text{CCH}_3)_6(3\text{-Me-py})_3](\text{S})$ at 298 K where S is CH_3CN or Toluene

	CH_3CN solvate	toluene solvate
T, K	298	298
space group	$P2_1/c$	$P\bar{1}$
a, Å	12.760 (5)	13.056 (4)
b, Å	26.233 (11)	15.902 (3)
c, Å	14.819 (5)	12.896 (2)
α , deg	90.0	102.82 (2)
β , deg	116.20 (3)	118.96 (2)
γ , deg	90.0	70.02 (2)
d_{calcd} , g/cm ³	1.281	1.375
formula wt	858.25	909.34
Z	4	2
crystal size, mm	$0.36 \times 0.42 \times 0.56$	$0.38 \times 0.50 \times 0.62$
$F(000)$, electrons	1776.0	944.0
mode	$2\theta/\theta$	ω/θ
scan rate, deg/min	2–20	3–16
absorption coeff, μ , cm ⁻¹	10.19	10.36
transmission factor range	0.665–0.745	0.618–0.721
2θ range, deg	3–55	2–46
total reflections	11275 ($\pm h \pm k \pm l$)	7059 ($+h \pm k \pm l$)
$I > 2.58(I)$	3682	4619
no. of variables	390	321
ignorance factor, p	0.04	0.02
R	0.074	0.058
R_w	0.098	0.075
max shift/esd	0.081	0.114

for the solvent molecule) were transformed from previously determined coordinates in the $A\bar{1}$ space lattice of the 3-Me-py solvate into the conventional reduced $P\bar{1}$ setting and allowed to refine for several cycles of least squares. A subsequent difference Fourier synthesis revealed that the toluene solvate molecule was severely disordered as was the methylpyridine solvate molecule in the previous case. The positions of the methyl carbons on two of the Fe-bound pyridine rings were also disordered in a manner similar to that of the previous structure. The model for the final cycle of least squares was as follows: all atomic positions for the trimer were independently refined with anisotropic thermal coefficients for the iron, oxygen, and nitrogen atoms, and group isotropic thermal parameters were varied for the disordered pairs C(18) and C(24) along with a site occupancy factor for each (0.706 (10) and 0.581 (10) for "A" positions, respectively); positions for the aromatic carbon atoms of the two disordered solvate molecules were "ideally" constrained with one isotropic thermal parameter and site occupancy factor varied for the group (0.576 (8) for group "A"); positions for the methyl carbon atoms of the toluene solvate were allowed to vary independently with isotropic thermal coefficients tied to the solvate molecule group parameter; and, all hydrogen atoms were fixed in "idealized" positions linked with the appropriate occupancy factors and a single isotropic thermal parameter was refined for this group. Successful convergence was indicated by the maximum shift/error for the last cycle of 0.114. The one peak above background in the final difference Fourier map was located on an inversion center isolated from the rest of the atoms in the crystal. The density of this peak was considerably less than $1 \text{ e}/\text{\AA}^3$, and the remainder of the map had no significant features. There were no obvious systematic errors among the final observed and calculated structure factors.

The final positional parameters for all refined atoms can be found in Table V. Listings of the hydrogen atom coordinates, thermal parameters, and observed and calculated structure factors are available in the supplementary material.

Crystal Measurements, Data Collection, and Structure Solution and Refinement for $[\text{Fe}_3\text{O}(\text{O}_2\text{CCH}_3)_6(3\text{-Me-py})_3](\text{CH}_3\text{CN})$. The opaque, blue, prismatic crystal used for data collection was roughly equidimensional with several distinct faces as well as some damaged and striated faces. The sample was bound by the following inversion related forms: $\{0\ 1\ \bar{1}\}$, $\{0\ 1\ 1\}$, $\{0\ 1\ 0\}$, and $\{1\ 0\ 0\}$. The interfacial separations between inversion-related faces were 0.36, 0.42, 0.44, and 0.56 mm, respectively. The sample was mounted in a thin-walled tapered glass capillary under inert conditions with the (20–1) scattering planes roughly normal to the spindle axis.

Data collection at the University of Illinois was carried out at 298 K on a Syntex $P2_1$ automated four-circle diffractometer. The unit cell parameters, listed in Table III, were obtained by a least-squares fit to the automatically centered settings for 15 reflections. Details of the data collection may also be found in Table IV. There was no remarkable change in the appearance of the crystal during the experiment; however, there was a considerable loss of intensity (43% loss of intensity by the

Table V. Positional Parameters for $[\text{Fe}_3\text{O}(\text{O}_2\text{CCH}_3)_6(3\text{-Me-py})_3](\text{C}_7\text{H}_8)$ at 298 K

	x/a	y/b	z/c
Fe1	0.23382 (7)	0.23152 (6)	-0.19602 (7)
Fe2	0.29581 (7)	0.26539 (6)	0.08504 (7)
Fe3	0.49052 (7)	0.28085 (6)	0.00165 (7)
O	0.3390 (3)	0.2587 (3)	-0.0368 (3)
O1	0.0796 (3)	0.3194 (3)	-0.1901 (3)
O2	0.1167 (3)	0.3395 (3)	-0.0003 (3)
O3	0.3372 (4)	0.3828 (3)	0.1669 (4)
O4	0.4759 (4)	0.3911 (3)	0.1192 (4)
O5	0.4095 (4)	0.3682 (3)	-0.1315 (4)
O6	0.2436 (4)	0.3294 (3)	-0.2688 (4)
O7	0.1989 (4)	0.1267 (3)	-0.1611 (3)
O8	0.2414 (4)	0.1501 (3)	0.0303 (3)
O9	0.4618 (3)	0.1898 (3)	0.1946 (3)
O10	0.5978 (3)	0.1974 (3)	0.1423 (4)
O11	0.5369 (3)	0.1719 (3)	-0.1057 (4)
O12	0.3636 (4)	0.1383 (3)	-0.2373 (4)
N1	0.1043 (4)	0.2018 (3)	-0.3844 (4)
N2	0.2528 (4)	0.2714 (3)	0.2357 (4)
N3	0.6626 (4)	0.3058 (3)	0.0372 (4)
C1	0.0505 (5)	0.3534 (4)	-0.1078 (5)
C2	-0.0758 (7)	0.4142 (5)	-0.1419 (7)
C3	0.4109 (6)	0.4196 (4)	0.1726 (5)
C4	0.4222 (7)	0.5047 (5)	0.2506 (7)
C5	0.3152 (6)	0.3776 (4)	-0.2276 (6)
C6	0.2860 (7)	0.4499 (5)	-0.3015 (7)
C7	0.2120 (6)	0.1054 (4)	-0.0669 (6)
C8	0.1884 (7)	0.0176 (5)	-0.0727 (6)
C9	0.5659 (6)	0.1684 (4)	0.2016 (5)
C10	0.6624 (6)	0.1001 (5)	0.2903 (6)
C11	0.4763 (6)	0.1245 (4)	-0.1899 (6)
C12	0.5477 (7)	0.0434 (5)	-0.2365 (7)
C13	0.0139 (6)	0.2660 (4)	-0.4487 (6)
C14	-0.0682 (6)	0.2496 (5)	-0.5691 (6)
C15	-0.0538 (7)	0.1671 (5)	-0.6182 (7)
C16	0.0380 (8)	0.0987 (6)	-0.5570 (8)
C17	0.1185 (7)	0.1199 (5)	-0.4334 (7)
C18a	-0.165 (1)	0.3251 (8)	-0.635 (1)
C18b	0.056 (3)	0.017 (2)	-0.605 (2)
C19	0.2961 (6)	0.2010 (4)	0.2985 (6)
C20	0.2740 (7)	0.2034 (5)	0.3958 (6)
C21	0.2071 (7)	0.2811 (5)	0.4258 (7)
C22	0.1595 (7)	0.3546 (5)	0.3614 (7)
C23	0.1876 (6)	0.3469 (4)	0.2671 (6)
C24a	0.327 (1)	0.118 (1)	0.457 (1)
C24b	0.068 (2)	0.439 (1)	0.376 (2)
C25	0.7629 (6)	0.2383 (4)	0.0577 (5)
C26	0.8734 (6)	0.2490 (5)	0.0766 (6)
C27	0.8742 (7)	0.3334 (5)	0.0733 (6)
C28	0.7740 (7)	0.4044 (5)	0.0548 (6)
C29	0.6676 (6)	0.3878 (5)	0.0351 (6)
C30	0.9823 (8)	0.1692 (6)	0.0995 (8)
C31a	0.635 (1)	0.2732 (10)	0.583 (1)
C32a	0.752 (1)	0.2507 (10)	0.591 (1)
C33a	0.850 (1)	0.1979 (10)	0.681 (1)
C34a	0.832 (1)	0.1675 (10)	0.762 (1)
C35a	0.715 (1)	0.1900 (10)	0.754 (1)
C36a	0.617 (1)	0.2428 (10)	0.665 (1)
C37a	0.532 (2)	0.321 (1)	0.483 (2)
C31b	0.639 (2)	0.285 (2)	0.527 (2)
C32b	0.756 (2)	0.245 (2)	0.610 (2)
C33b	0.773 (2)	0.214 (2)	0.712 (2)
C34b	0.673 (2)	0.224 (2)	0.731 (2)
C35b	0.556 (2)	0.265 (2)	0.648 (2)
C36b	0.539 (2)	0.295 (2)	0.546 (2)
C37b	0.609 (3)	0.337 (2)	0.453 (2)

end of shell 2). Correction for crystal decay was made as a function of the behavior of standard intensities measured at regular intervals during the experiment and applied in an isotropic manner. Corrections were also made to the data for Lorentz and polarization effects and for anomalous dispersion effects. A numerical absorption correction was applied where the maximum and minimum transmission factors were 0.745 and 0.665.

The structure was solved by direct methods (MULTAN); correct positions for the three iron atoms and the central oxygen atom were deduced from an E map. A weighted difference Fourier map revealed positions for all but three of the remaining non-hydrogen atoms and subsequent

Table VI. Positional Parameters for $[\text{Fe}_3\text{O}(\text{O}_2\text{CCH}_3)_6(3\text{-Me-py})_3](\text{CH}_3\text{CN})$ at 298 K

atom	x/a	y/b	z/c
Fe1	-0.1524 (1)	0.17714 (5)	0.5740 (1)
Fe2	0.1165 (1)	0.14336 (5)	0.6263 (1)
Fe3	-0.0338 (1)	0.08105 (5)	0.7270 (1)
O	-0.0248 (5)	0.1343 (2)	0.6428 (5)
O1	-0.1494 (7)	0.1732 (3)	0.4381 (5)
O2	0.0313 (7)	0.1503 (3)	0.4710 (6)
O3	0.1442 (6)	0.0675 (3)	0.6114 (6)
O4	0.0407 (6)	0.0264 (3)	0.6750 (6)
O5	-0.1962 (6)	0.0547 (3)	0.6264 (6)
O6	-0.2751 (6)	0.1207 (3)	0.5259 (6)
O7	-0.0599 (7)	0.2443 (3)	0.6092 (6)
O8	0.1201 (7)	0.2216 (3)	0.6374 (7)
O9	0.2239 (6)	0.1422 (3)	0.7820 (6)
O10	0.1230 (7)	0.0994 (3)	0.8467 (5)
O11	-0.1131 (7)	0.1250 (3)	0.7967 (6)
O12	-0.1858 (7)	0.1918 (3)	0.6935 (6)
C1	-0.071 (1)	0.1619 (4)	0.4123 (9)
C2	-0.105 (1)	0.1631 (6)	0.3015 (9)
C3	0.1058 (9)	0.0275 (4)	0.6323 (8)
C4	0.136 (1)	-0.0235 (5)	0.602 (1)
C5	-0.2756 (9)	0.0755 (5)	0.5519 (9)
C6	-0.384 (1)	0.0450 (5)	0.489 (1)
C7	0.045 (1)	0.2532 (4)	0.6314 (9)
C8	0.082 (1)	0.3078 (5)	0.651 (2)
C9	0.1992 (10)	0.1303 (5)	0.8516 (10)
C10	0.264 (2)	0.1571 (8)	0.952 (1)
C11	-0.159 (1)	0.1678 (5)	0.7753 (10)
C12	-0.191 (2)	0.1952 (5)	0.850 (1)
N1	-0.3068 (8)	0.2276 (4)	0.4916 (8)
C13	-0.393 (1)	0.2138 (6)	0.405 (1)
C14	-0.491 (1)	0.2452 (8)	0.352 (1)
C15	-0.492 (2)	0.2917 (7)	0.395 (2)
C16	-0.407 (2)	0.3035 (8)	0.477 (1)
C17	-0.319 (1)	0.2738 (6)	0.523 (1)
C18	-0.580 (2)	0.2232 (9)	0.259 (2)
N2	0.2810 (8)	0.1527 (3)	0.6107 (7)
C19	0.3705 (9)	0.1239 (5)	0.6631 (9)
C20	0.479 (1)	0.1261 (6)	0.657 (1)
C21	0.486 (1)	0.1613 (7)	0.595 (1)
C22	0.397 (1)	0.1916 (6)	0.538 (1)
C23	0.290 (1)	0.1869 (5)	0.549 (1)
C24	0.577 (1)	0.0913 (7)	0.721 (1)
N3	-0.0408 (8)	0.0167 (3)	0.8228 (6)
C25	0.049 (1)	-0.0139 (4)	0.8668 (8)
C26	0.050 (1)	-0.0548 (5)	0.9264 (9)
C27	-0.046 (2)	-0.0645 (5)	0.9391 (10)
C28	-0.140 (1)	-0.0341 (6)	0.891 (1)
C29	-0.137 (1)	0.0065 (5)	0.8334 (8)
C30a	0.163 (3)	-0.0852 (9)	0.978 (2)
C30b	-0.253 (4)	-0.042 (1)	0.893 (3)
N4	0.337 (1)	0.0946 (8)	0.331 (1)
C31	0.267 (2)	0.0864 (7)	0.355 (1)
C32	0.177 (1)	0.0733 (5)	0.380 (1)

least-squares difference Fourier calculations gave positions for these last three atoms including two disordered positions for atom C30. In the final block diagonalized cycle of least squares, all non-hydrogen atoms were refined with anisotropic thermal coefficients, a group isotropic thermal parameter was refined for the hydrogen atoms, and an empirical isotropic extinction parameter was varied ($1.7(2) \times 10^{-7}$). Successful convergence was indicated by the maximum shift over error for the last cycle, 0.081; there were several high correlation coefficients. The final difference Fourier had fourteen peaks above background in a relatively clustered section of the map near an inversion center. These residual peaks presented no distinct pattern but appeared to be three partially occupied solvate molecule sites. Efforts to resolve this disorder were unsuccessful. There were no apparent systematic errors between the final observed and calculated structure factors.

The final positional parameters for all refined atoms can be found in Table VI. Listings of the hydrogen atom coordinates, thermal parameters, and observed and calculated structure factors are available in the supplementary material.

Results and Discussion

^{57}Fe Mössbauer Data. Variable-temperature Mössbauer spectra were run for the four complexes of composition $[\text{Fe}_3\text{O}$ -

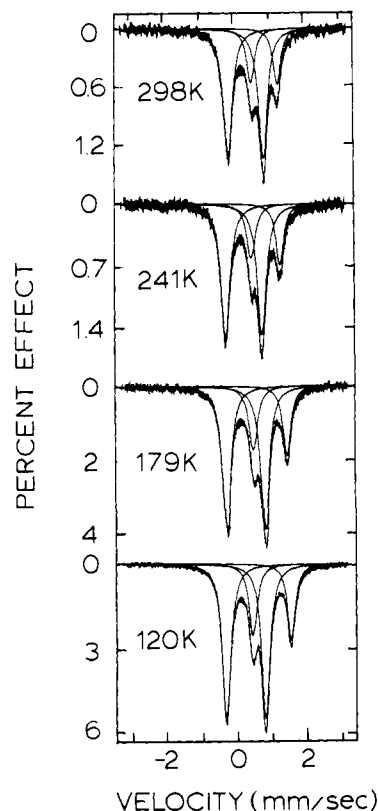


Figure 1. Variable-temperature ^{57}Fe Mössbauer spectra for $[\text{Fe}_3\text{O}(\text{O}_2\text{CCH}_3)_6(3\text{-Me-py})_3](\text{CH}_3\text{CN})$ (1).

$(\text{O}_2\text{CCH}_3)_6(3\text{-Me-py})_3\cdot\text{S}$, where $\text{S} = \text{CH}_3\text{CN}$ (1), toluene (2), 3-methylpyridine (3), and benzene (4). It will be shown that 1 has valence-trapped electronic states from 120 to 298 K on the Mössbauer time scale. The other three complexes will be shown to be valence trapped below ~ 100 K, whereas increasing the temperature above ~ 100 K leads to an increase in the effective electron-transfer rate in these three complexes such that at temperatures above ~ 300 K the rate is in excess of $\sim 10^7$ s^{-1} .

In Figure 1 are illustrated Mössbauer spectra for the CH_3CN solvate 1 taken in the range of 120–300 K. Least-squares fitting of the spectra to Lorentzian line shapes (solid lines) clearly indicates that each spectrum is comprised of only two quadrupole-split doublets. Table VII summarizes the Mössbauer fitting parameters. In each spectrum the more intense doublet corresponds to the two high-spin Fe^{III} ions in complex 1 and the less intense doublet is for the one Fe^{II} ion. It is clear that throughout the range of 120–298 K complex 1 is valence trapped on the Mössbauer time scale. The area ratio of $\text{Fe}^{\text{III}}:\text{Fe}^{\text{II}}$ signals is 1.96 at 120 K and increases slightly to 2.27 at 300 K. It is not unreasonable to expect a high-spin Fe^{III} ion to experience a recoilless fraction that is somewhat larger than that of a high-spin Fe^{II} ion in the same molecule at 300 K.

The center shifts (δ) and quadrupole splittings (ΔE_Q) for the two doublets in the spectrum of 1 decrease as the temperature is increased; the changes are small for the Fe^{III} doublet, whereas they are somewhat larger for the Fe^{II} doublet. However, these changes are normal and do not reflect the onset of intramolecular electron transfer. The decrease in center shift values with increasing temperature is due to the second-order Doppler shift.⁴² In the case of the Fe^{II} ion the temperature dependence seen in ΔE_Q results from the thermal population of low-lying excited states which result from the spin-orbit splitting of the $^5\text{T}_2$ state.⁴³ It

(42) Greenwood, N. N.; Gibb, T. C. *Mössbauer Spectroscopy*; Chapman and Hall Ltd.: London, 1971.

(43) (a) Timken, M. D.; Marritt, W. A.; Hendrickson, D. N.; Gagné, R. A.; Sinn, E. *Inorg. Chem.* **1985**, *24*, 4202. (b) Gülich, P.; Link, R.; Trautwein, A. *Mössbauer Spectroscopy and Transition Metal Chemistry*; Springer-Verlag: New York, 1978; pp 73–75.

Table VII. ^{57}Fe Mössbauer Fitting Parameters for $[\text{Fe}_3\text{O}(\text{O}_2\text{CCH}_3)_6(3\text{-Me-py})_3](\text{CH}_3\text{CN})^a$

T, K	$\delta,^b$ mm/s		$\Delta E_Q,^c$ mm/s		$\Gamma,^c$ mm/s		area ratio ^d
	Fe ^{III}	Fe ^{II}	Fe ^{III}	Fe ^{II}	Fe ^{III}	Fe ^{II}	
120 (1)	0.542 (1)	1.292 (1)	1.126 (1)	1.109 (2)	0.142 (1) 0.143 (1)	0.140 (2) 0.133 (2)	1.96 (2)
179 (1)	0.539 (1)	1.244 (2)	1.096 (2)	0.965 (3)	0.147 (3) 0.147 (2)	0.147 (3) 0.135 (3)	1.99 (3)
241 (1)	0.536 (2)	1.159 (3)	1.039 (3)	0.825 (7)	0.152 (3) 0.156 (3)	0.149 (7) 0.133 (6)	2.14 (3)
298 (1)	0.530 (1)	1.077 (3)	1.005 (3)	0.753 (6)	0.157 (3) 0.153 (3)	0.136 (6) 0.132 (6)	2.27 (5)

^a Peaks were least-squares fit to Lorentzian line shapes with equal areas for both components of a doublet. The error in the last significant figure is given in parentheses. ^b Center shifts relative to iron metal. ^c Half-width at half-maximum listed in order of increasing velocity of the peak. ^d Area ratio of Fe^{III}/Fe^{II}.

Table VIII. ^{57}Fe Mössbauer Fitting Parameters for $[\text{Fe}_3\text{O}(\text{O}_2\text{CCH}_3)_6(3\text{-Me-py})_3](\text{toluene})$

T, K	$\Delta E_Q,^c$ mm/s			$\delta,^b$ mm/s			$\Gamma,^c$ mm/s			percentage of area		
	Fe ^{III}	Fe ^{av}	Fe ^{II}	Fe ^{III}	Fe ^{av}	Fe ^{II}	Fe ^{III}	Fe ^{av}	Fe ^{II}	Fe ^{III}	Fe ^{av}	Fe ^{II}
5.8	1.090 (1)		1.829 (2)	0.542 (1)		1.250 (1)	0.140 (1) 0.134 (1)		0.178 (2) 0.163 (2)	65.8 (1)		34.2 (1)
26	1.087 (1)		1.715 (3)	0.539 (1)		1.252 (1)	0.140 (1) 0.137 (1)		0.188 (3) 0.174 (2)	64.4 (1)		35.6 (1)
49	1.069 (1)		1.641 (2)	0.540 (1)		1.243 (1)	0.142 (1) 0.138 (1)		0.194 (2) 0.180 (2)	62.2 (1)		37.8 (1)
62	1.047 (1)		1.562 (3)	0.547 (1)		1.211 (2)	0.164 (1) 0.161 (1)		0.232 (3) 0.241 (4)	62.4 (1)		37.6 (1)
71	1.035 (1)	1.083 (19)	1.467 (9)	0.549 (1)	0.861 (10)	1.201 (5)	0.160 (2) 0.155 (2)	0.215 (26) 0.323 (39)	0.268 (8) 0.253 (6)	55.4 (1)	15.8 (1)	28.8 (1)
88	1.016 (2)	1.007 (5) 0.833 (3)	1.267 (10)	0.560 (1) 0.662 (1)	0.798 (3)	1.087 (5)	0.135 (4) 0.119 (4)	0.268 (10) 0.291 (9)	0.177 (8) 0.207 (8)	52.4 (1)	22.5 (2)	25.1 (1)
324								0.165 (2) 0.151 (2)				

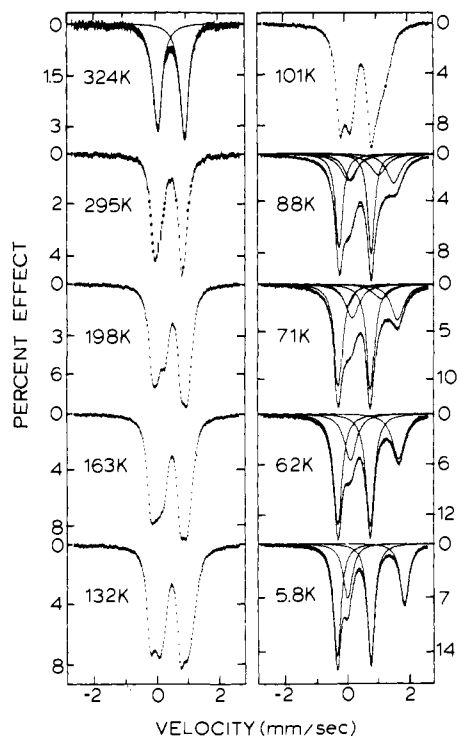


Figure 2. Variable-temperature ^{57}Fe Mössbauer spectra for $[\text{Fe}_3\text{O}(\text{O}_2\text{CCH}_3)_6(3\text{-Me-py})_3](\text{toluene})$ (2).

is clear that **1** is valence trapped at 298 K.

In contrast to the behavior of **1**, the other three solvates **2**, **3**, and **4** give Mössbauer spectra which have a pronounced temperature dependence. As can be seen in Figures 2-4, the Mössbauer characteristics of these other three solvates are similar in the range of 4.2-300 K. At liquid-helium temperature the spectra of all three complexes have two doublets in the area ratio

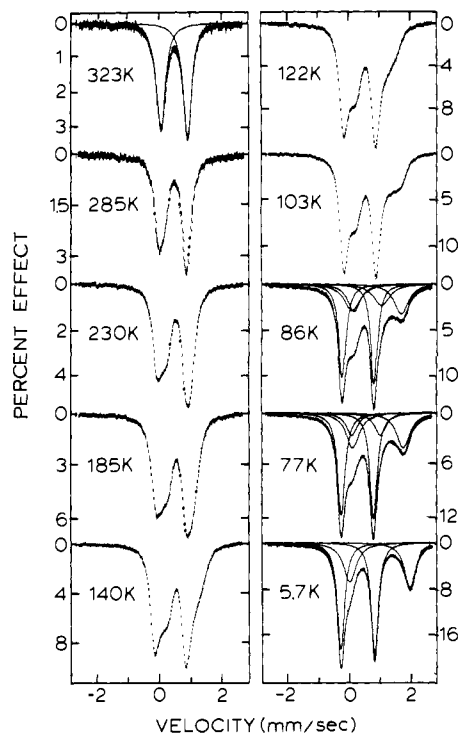
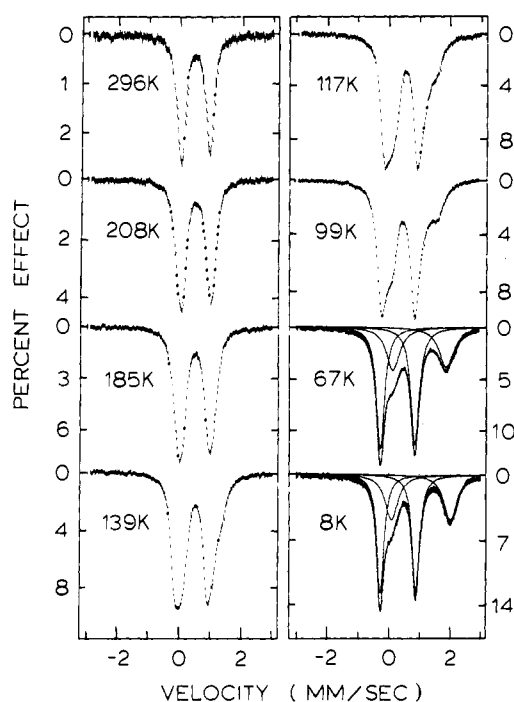


Figure 3. Variable-temperature ^{57}Fe Mössbauer spectra for $[\text{Fe}_3\text{O}(\text{O}_2\text{CCH}_3)_6(3\text{-Me-py})_3](3\text{-Me-py})$ (3).

of 2:1, one is characteristic of high-spin Fe^{III} and the other high-spin Fe^{II} (see Tables VIII and IX for parameters). The three complexes are valence trapped on the Mössbauer time scale at these low temperatures. However, all three complexes show a single doublet at room temperature. The δ and ΔE_Q values for this doublet indicate it is the signal neither for a high-spin Fe^{III} ion nor for a high-spin Fe^{II} ion. The characteristics of this room

Table IX. ^{57}Fe Mössbauer Fitting Parameters for $[\text{Fe}_3\text{O}(\text{O}_2\text{CCH}_3)_6(3\text{-Me-py})_3]\cdot\text{S}$, Where S Is 3-Me-py or Benzene

T, K	ΔE_Q , mm/s			δ , mm/s			Γ , mm/s			percentage of area		
	Fe^{III}	Fe^{av}	Fe^{II}	Fe^{III}	Fe^{av}	Fe^{II}	Fe^{III}	Fe^{av}	Fe^{II}	Fe^{III}	Fe^{av}	Fe^{II}
$[\text{Fe}_3\text{O}(\text{O}_2\text{CCH}_3)_6(3\text{-Me-py})_3](3\text{-Me-py})$												
5.7	1.095 (1)		1.942 (4)	0.546 (1)		1.258 (2)	0.141 (1)		0.250 (5)	65.4 (2)		34.6 (1)
							0.134 (1)		0.217 (4)			
37	1.088 (1)		1.807 (4)	0.544 (1)		1.252 (2)	0.139 (1)		0.259 (4)	65.6 (2)		34.4 (1)
							0.135 (1)		0.232 (4)			
58	1.066 (1)		1.720 (4)	0.542 (1)		1.243 (2)	0.147 (1)		0.266 (4)	61.4 (2)		38.6 (1)
							0.141 (1)		0.243 (4)			
77	1.045 (1)	0.962 (47)	1.620 (28)	0.545 (1)	0.837 (24)	1.211 (14)	0.145 (3)	0.219 (19)	0.251 (28)	55.4 (2)	17.0 (1)	27.6 (1)
							0.139 (2)	0.221 (23)	0.259 (7)			
86	1.032 (2)	0.893 (35)	1.594 (43)	0.550 (1)	0.853 (18)	1.143 (21)	0.139 (3)	0.247 (23)	0.310 (45)	51.4 (2)	24.2 (1)	24.4 (1)
							0.131 (3)	0.317 (23)	0.275 (10)			
323		0.861 (2)			0.688 (1)			0.175 (2)				
								0.162 (2)				
$[\text{Fe}_3\text{O}(\text{O}_2\text{CCH}_3)_6(3\text{-Me-py})_3](\text{C}_6\text{H}_6)$												
8	1.156 (1)		1.915 (1)	0.561 (1)		1.294 (2)	0.140 (1)		0.253 (4)	60.0 (2)		40.0 (4)
							0.141 (1)		0.245 (5)			
67	1.131 (1)		1.743 (4)	0.566 (1)		1.276 (2)	0.159 (1)		0.267 (4)	63.1 (2)		36.9 (2)
							0.169 (1)		0.288 (5)			

**Figure 4.** Variable-temperature ^{57}Fe Mössbauer spectra for $[\text{Fe}_3\text{O}(\text{O}_2\text{CCH}_3)_6(3\text{-Me-py})_3](\text{benzene})$ (4).

temperature doublet are only consistent with a rate of intramolecular electron transfer in each Fe_3O complex greater than $\sim 10^7 \text{ s}^{-1}$. The single doublet is an average signal for all three iron ions in the Fe_3O complex. It is evident in Tables VIII and IX that the line widths of the "average-valence" doublet for **2**, and **3**, are somewhat larger than the instrumental line widths of 0.12–0.16 mm/s. This indicates that the valences are not completely delocalized on the Mössbauer time scale at room temperature.

The Mössbauer temperature dependencies illustrated in Figures 2, 3, and 4 for complexes **2**, **3**, and **4**, respectively, can be qualitatively described in each case as two doublets at low temperature, which in response to an increase in temperature move together to become a single doublet at high temperature. The similarities in temperature dependencies will be shown below to be a natural consequence of the fact that **2**, **3**, and **4** are isostructural. Closer examination of the spectra in Figures 2, 3, and 4 reveals additional facts. First, it has not proven possible to develop unique fits of intermediate-temperature spectra with Lorentzian line shapes. Second, the benzene solvate **4** converts to a valence-detraped mode on the Mössbauer time scale at a lower temperature than the other two solvates. Third, it is clear that the spectra for the

3-Me-py and toluene solvates show the appearance of a third quadrupole-split doublet at ~ 70 to 80 K . That is, it is not possible to fit the spectra with just two doublets. Fittings to three doublets are illustrated in Figures 2 and 3. In the case of the benzene solvate perhaps the spectrum is collapsing to an "average-valence" doublet at too low a temperature to readily see this third doublet.

It has been proposed in several theoretical papers^{44–47} that there could be a temperature region for these mixed-valence Fe_3O acetate complexes where complexes in electronically localized and delocalized states coexist. In one theoretical paper⁴⁷ there is, in fact, a discussion not only of the electronic structure of an isolated Fe_3O complex but also of the different possible phase transitions. The ground-state potential-energy surface for a trinuclear mixed-valence complex can have one, three, or four minima depending on the magnitude of Δ which is equal to kw/λ^2 , where w is the electron-transfer integral between two iron ions, k is the force constant for the vibrational distortion mode which is active in the electron transfer, and λ is the vibronic coupling constant of the d-electronic states with the distortion.⁴⁷ When $\Delta > 0.765$, there is only one minimum in the ground-state surface and the Fe_3O complex has no barrier for electron transfer—it is electronically delocalized. When $0 < \Delta < 2/3$, there are three minima in the ground-state surface. These three minima correspond to the three possible electronically localized states, i.e., $\text{Fe}_A^{\text{II}}\text{Fe}_B^{\text{III}}\text{Fe}_C^{\text{III}}$, $\text{Fe}_A^{\text{III}}\text{Fe}_B^{\text{II}}\text{Fe}_C^{\text{III}}$, or $\text{Fe}_A^{\text{III}}\text{Fe}_B^{\text{III}}\text{Fe}_C^{\text{II}}$. Finally, when $2/3 < \Delta < 0.765$, four minima exist in the ground-state potential-energy surface. In addition to the three electronically localized states, the fourth minimum corresponds to a complex in an electronically delocalized state where all three iron ions are equivalent. Depending on the energy difference between this fourth state and the other three states, Fe_3O complexes can be in this delocalized state. In a Mössbauer study³³ of mixed-valence $[\text{Fe}_3\text{O}(\text{O}_2\text{CCH}_3)_6(\text{py})_3](\text{py})$, a doublet assigned to complexes in this electronically delocalized state was seen to appear at $\sim 112 \text{ K}$. This is particularly interesting in view of the fact that heat-capacity measurements³³ show there is a first-order phase transition at this same temperature.

For the toluene solvate **2** a doublet with spectral parameters appropriate for this electronically delocalized state appears at $\sim 71 \text{ K}$. This doublet was found to have 15.8% of the spectral area at 71 K , a value that increases slightly to 22.5% at 88 K . Although it is not easy to get a unique fit of the spectra in the 101–163 K range, the relative intensity of the " Fe^{II} " signal indicates that

(44) Launay, J. P.; Babonneau, F. *Chem. Phys.* **1982**, *67*, 295.(45) Borshch, S. A.; Kotov, I. N.; Bersuker, I. B. *Chem. Phys. Lett.* **1982**, *89*, 381.(46) Cannon, R. D.; Montri, L.; Brown, D. B.; Marshall, K. M.; Elliot, C. M. *J. Am. Chem. Soc.* **1984**, *106*, 2591.(47) Kambara, T.; Hendrickson, D. N.; Sorai, M.; Oh, S. M. *J. Chem. Phys.* **1986**, *85*, 2895–2909.

Table X. Distances and Angles of the Central Atoms for $[\text{Fe}_3\text{O}(\text{O}_2\text{CCH}_3)_6(3\text{-Me-py})_3](\text{CH}_3\text{CN})$ at 298 K

atoms	distance, Å	atoms	distance, Å
Fe(1)-O	1.867 (6)	Fe(1)-N(1)	2.236 (10)
Fe(2)-O	1.937 (6)	Fe(2)-N(2)	2.225 (9)
Fe(3)-O	1.910 (6)	Fe(3)-N(3)	2.233 (8)
Fe(1)-Fe(2)	3.287 (2)	Fe(1)-O ^a	2.041 (7)
Fe(1)-Fe(3)	3.279 (2)	Fe(2)-O ^a	2.071 (8)
Fe(2)-Fe(3)	3.332 (2)	Fe(3)-O ^a	2.065 (8)
atoms	angle, deg	atoms	angle, deg
Fe(1)-O-Fe(2)	119.5 (3)	Fe(1)-Fe(2)-Fe(3)	59.39 (4)
Fe(1)-O-Fe(3)	120.5 (3)	Fe(1)-Fe(3)-Fe(2)	59.63 (4)
Fe(2)-O-Fe(3)	120.0 (3)	Fe(2)-Fe(1)-Fe(3)	60.98 (4)
O-Fe(1)-N(1)	179.2 (3)	Fe ₃ O-L ₁ ^b	82.8
O-Fe(2)-N(2)	178.6 (3)	Fe ₃ O-L ₂ ^b	3.7
O-Fe(3)-N(3)	177.7 (3)	Fe ₃ O-L ₃ ^b	3.1

^a Average distance between metal and oxygen atoms of the acetate groups. ^b Dihedral angle between the Fe₃O plane and the 3-Me-py ring.

complexes which are delocalized are present in this range as well.

The doublet corresponding to complexes in the electronically delocalized state is also present in the Mössbauer spectra of the 3-Me-py solvate (3). The spectral area of this third doublet for 3 is 17.0% at 77 K and 24.2% at 86 K. In the temperature range of 103–185 K, this third doublet is clearly superimposed on the “Fe^{II}” and “Fe^{III}” doublets.

It is suggested that the temperature dependence seen in the Mössbauer spectra for 2, 3, and 4 is not just the result of thermally activating these mixed-valence complexes to overcome a potential-energy barrier for electron transfer. Rather, it is suggested that some part of the temperature dependence is due to the onset of lattice dynamics at various temperatures. In fact, as will be elaborated on in a forthcoming paper,⁴⁸ heat-capacity measurements for the 3-Me-py solvate 3 show the presence of phase transitions at 181, 263.5, 271.5, and 282.5 K. It is likely that there are in the solid state intermolecular interactions between Fe₃O complexes, intermolecular interactions that are propagated perhaps by the solvate molecules. Thus, when the thermal energy becomes greater than these intermolecular interactions in the crystal lattice, the intermolecular interactions will be modulated by thermal motion. For a given Fe₃O complex this could lead to a change in the ground-state potential-energy surface. The parameter Δ ($=kw/\lambda^2$) is not changed, but what is changed is the nature of the intermolecular interactions. These interactions can, if they are asymmetrically disposed relative to a Fe₃O complex, introduce a zero-point energy difference between the four minima on the surface. That is, an “asymmetric” environment can lead to the case where one minimum is at much lower energy than the others and the Fe₃O complex is valence trapped.

Single-Crystal X-ray Structures of 1, 2, and 3. The molecular and crystal structures of the CH₃CN (1), toluene (2), and 3-Me-py (3) solvates were determined. The present and previous work^{32,33} has shown that changing the solvate molecule can have a dramatic effect on the rate of intramolecular electron transfer in these mixed-valence iron acetates. A comparison of the X-ray structure of valence-trapped 1 with those of isostructural valence-detraped 2 and 3 should provide insight about the nature of the solvate molecule control of the electron-transfer rate. The trinuclear mixed-valence Fe₃O complexes in 1, 2, and 3 are chemically identical; the only change from one complex to another is in the solvate molecule.

$[\text{Fe}_3\text{O}(\text{O}_2\text{CCH}_3)_6(3\text{-Me-py})_3](\text{CH}_3\text{CN})$ (1) crystallizes in the space group $P2_1/c$ with four molecules in the unit cell. A perspective view of the molecular structure is depicted in Figure 5A, and selected bond distances and angles are listed in Table X (a more complete list of bond distances and angles is available in the supplementary material). There is no crystallographically imposed symmetry for the Fe₃O complex. The planes of two of

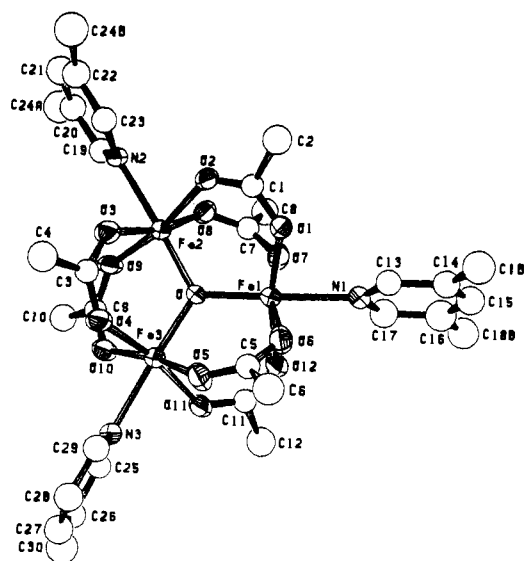
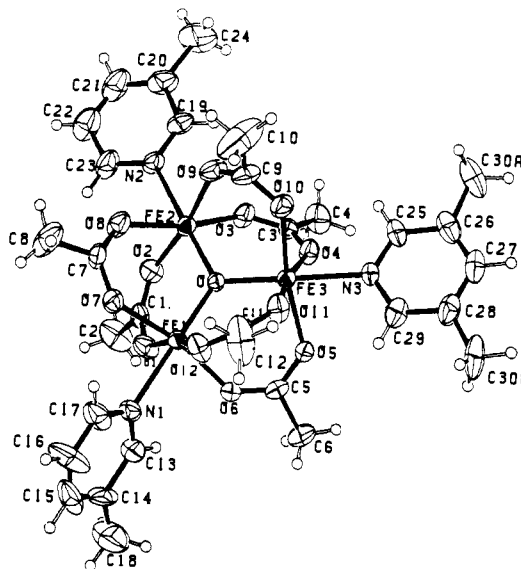


Figure 5. (A, top) Perspective view of the mixed-valence complex in $[\text{Fe}_3\text{O}(\text{O}_2\text{CCH}_3)_6(3\text{-Me-py})_3](\text{CH}_3\text{CN})$ (1). (B, bottom) Perspective view of the mixed-valence complex in $[\text{Fe}_3\text{O}(\text{O}_2\text{CCH}_3)_6(3\text{-Me-py})_3](\text{toluene})$ (2).

the three 3-Me-py ligands are nearly parallel to the Fe₃O plane, while the plane of the third ligand is nearly perpendicular to the Fe₃O plane; dihedral angles between 3-Me-py ligand planes and the Fe₃O plane are 3.7, 3.1, and 82.8°. One of the three 3-Me-py ligands is twofold disordered.

The toluene (2) and 3-Me-py (3) solvates are isostructural. $[\text{Fe}_3\text{O}(\text{O}_2\text{CCH}_3)_6(3\text{-Me-py})_3](\text{toluene})$ was refined in the space group $P\bar{1}$ with 2 formula units per cell. The structure of the 3-Me-py solvate was refined in the $A\bar{1}$ space group (nonstandard setting) with $Z = 4$. When the nonstandard setting is transformed to the standard $P\bar{1}$ cell, the lattice parameters of the 298 K structure of 3 (given in Table I) become $a = 13.052$ Å, $b = 15.939$ Å, $c = 12.887$ Å, $\alpha = 102.57^\circ$, $\beta = 119.26^\circ$, and $\gamma = 70.09^\circ$. These cell parameters are very close to those of the toluene solvate (see Table IV).

A perspective drawing of the 298 K molecular structure of the toluene solvate Fe₃O complex is shown in Figure 5B. Selected bond distances and angles are given in Table XI. As with complex 1, there is no crystallographically imposed symmetry for the Fe₃O complex in 2. Two of the three 3-Me-py ligands are twofold disordered. All three 3-Me-py ligands are coordinated to the iron ions with their molecular planes nearly perpendicular to the Fe₃O

(48) Sorai, M.; Shiomi, Y.; Hendrickson, D. N.; Oh, S. M. *Inorg. Chem.*, in press.

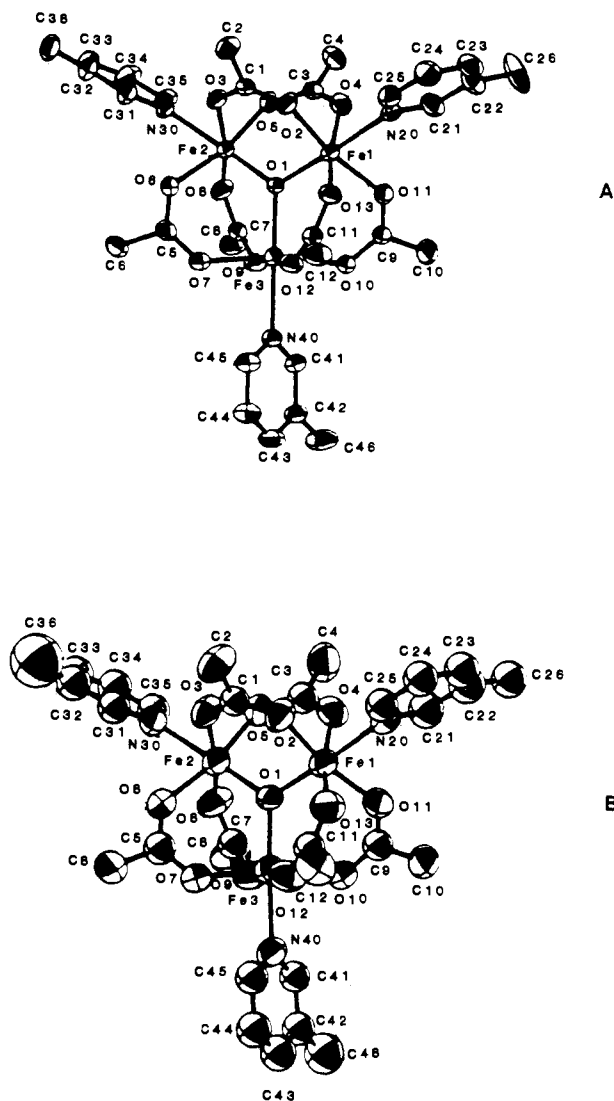


Figure 6. Perspective drawings of the mixed-valence complex in $[\text{Fe}_3\text{O}(\text{O}_2\text{CCH}_3)_6(3\text{-Me-py})_3](3\text{-Me-py})$ (**3**) at 128 K (A) and at 298 K (B). Disordered methyl carbon atoms C(27) and C(37) are bonded to C(24) and C(34), respectively.

plane; the dihedral angles are 84.6, 85.7, and 89.2°. According to the Mössbauer data (see Figure 2) the toluene solvate complex is not totally "Mössbauer delocalized" at 298 K. The dimensions of the Fe_3O complex in **2** at 298 K still show that this triangular complex is quite distorted from an equilateral triangle. The Fe–O(oxide) distances range from 1.882 (3) to 1.932 (3) Å. This

Table XI. Distances and Angles of the Central Atoms for $[\text{Fe}_3\text{O}(\text{O}_2\text{CCH}_3)_6(3\text{-Me-py})_3](\text{C}_7\text{H}_8)$ at 298 K

atoms	distance, Å	atoms	distance, Å
Fe(1)–O	1.890 (4)	Fe(1)–N(1)	2.246 (5)
Fe(2)–O	1.882 (3)	Fe(2)–N(2)	2.245 (4)
Fe(3)–O	1.932 (3)	Fe(3)–N(3)	2.223 (4)
Fe(1)–Fe(2)	3.267 (1)	Fe(1)–O ^a	2.050 (4)
Fe(2)–Fe(3)	3.297 (1)	Fe(2)–O ^a	2.047 (4)
Fe(1)–Fe(3)	3.314 (1)	Fe(3)–O ^a	2.076 (5)
atoms	angle, deg	atoms	angle, deg
Fe(1)–O–Fe(2)	120.1 (2)	Fe(1)–Fe(2)–Fe(3)	60.64 (3)
Fe(1)–O–Fe(3)	120.3 (2)	Fe(1)–Fe(3)–Fe(2)	59.23 (3)
Fe(2)–O–Fe(3)	119.7 (2)	Fe(2)–Fe(1)–Fe(3)	60.13 (3)
O–Fe(1)–N(1)	178.4 (2)	Fe ₃ O–L ₁ ^b	84.6
O–Fe(2)–N(2)	177.5 (2)	Fe ₃ O–L ₂ ^b	85.7
O–Fe(3)–N(3)	177.4 (2)	Fe ₃ O–L ₃ ^b	89.2

^a Average distance between metal and oxygen atoms of the acetate group. ^b Dihedral angle between the Fe_3O plane and the 3-Me-py ring.

0.050-Å range is smaller than the 0.070 Å observed for the three Fe–O(oxide) distances in the valence-trapped CH_3CN solvate **1**.

Perspective drawings of the 3-Me-py solvate **3** at 128 and 298 K are shown in Figure 6. There is no change in the space group for **3** from 128 to 298 K; however, the dimensions of the Fe_3O complex do change. Selected bond distances and angles are collected in Table XII.

Stereoscopic views of the packing arrangements in the CH_3CN (**1**) and toluene (**2**) solvates are shown in Figures 7 and 8, respectively. The packing pattern of the 3-Me-py solvate (**3**) is essentially the same as that for the toluene solvate. As can be seen in Figure 7, the Fe_3O complexes in **1** are arranged in a dimer-like fashion with two molecules of CH_3CN sandwiched between two Fe_3O complexes. The solid-state packing arrangement for the toluene solvate (and the 3-Me-py solvate) is quite different than that for **1**. In **2** the Fe_3O molecular units are arranged two-dimensionally in a layer and the toluene solvate molecule is located in a cavity made by three Fe_3O complexes. Thus, ignoring the inherent asymmetry of the 3-Me-py molecule, the "two-dimensional" packing arrangement of **2** has an approximate threefold symmetry axis (the *c* axis of the $A\bar{1}$ unit cell). Powder X-ray diffraction patterns were run at room temperature for the four complexes **1**, **2**, **3**, and **4** (see Figure 9). It was found that the benzene solvate **4** is isostructural to **2** and **3**. These three solvates have a more symmetric packing arrangement than is present in **1**.

There is one important point to make about the crystal structures of **2** and **3**. The solvate molecules, toluene in **2** and 3-Me-py in **3**, are disordered between two positions. In Figure 10 are shown stereoscopic views of these two disordered solvate molecules. Given the fact that toluene and 3-Me-py have similar shapes, it is curious that the details of the two solvate molecule disorderings are different. It is possible that the difference reflects

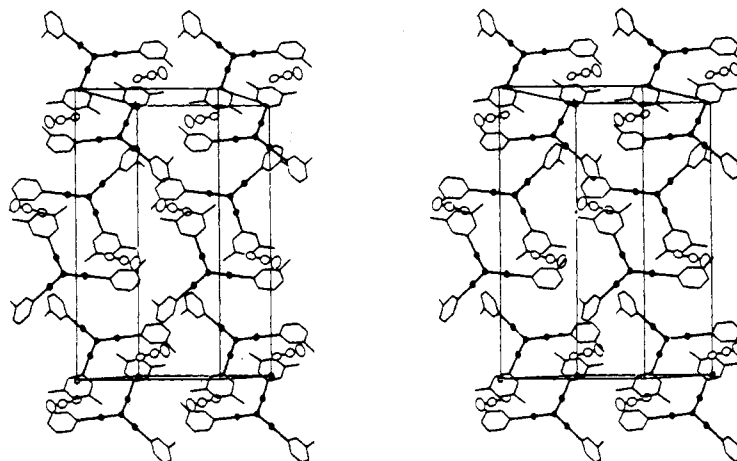


Figure 7. Stereoscopic view of the 298 K packing arrangement in $[\text{Fe}_3\text{O}(\text{O}_2\text{CCH}_3)_6(3\text{-Me-py})_3](\text{CH}_3\text{CN})$ (**1**).

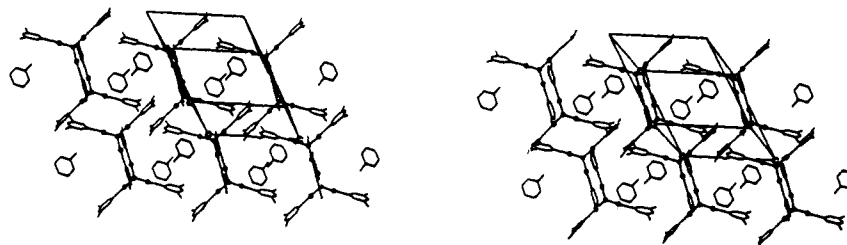


Figure 8. Stereoscopic view of the 298 K packing arrangement in $[\text{Fe}_3\text{O}(\text{O}_2\text{CCH}_3)_6(3\text{-Me-py})_3](\text{toluene})$ (2).

Table XII. Distances and Angles of the Central Atoms for $[\text{Fe}_3\text{O}(\text{O}_2\text{CCH}_3)_6(3\text{-Me-py})_3](3\text{-Me-py})$ at 128 and 298 K

atoms	distance, Å	
	128 K	298 K
Fe(1)–O(1)	1.916 (2)	1.888 (5)
Fe(2)–O(1)	1.855 (2)	1.897 (5)
Fe(3)–O(1)	1.936 (2)	1.921 (5)
Fe(1)–N(20)	2.230 (3)	2.266 (7)
Fe(2)–N(30)	2.235 (2)	2.243 (7)
Fe(3)–N(40)	2.216 (3)	2.237 (6)
Fe(1)–O ^a	2.060 (3)	2.045 (6)
Fe(2)–O ^a	2.036 (3)	2.046 (6)
Fe(3)–O ^a	2.075 (3)	2.066 (6)
Fe(1)–Fe(2)	3.272 (1)	3.279 (3)
Fe(1)–Fe(3)	3.326 (1)	3.305 (2)
Fe(2)–Fe(3)	3.287 (1)	3.299 (2)

atoms	angle, deg	
	128 K	298 K
Fe(1)–O(1)–Fe(2)	120.3 (1)	120.2 (2)
Fe(1)–O(1)–Fe(3)	119.4 (1)	120.2 (2)
Fe(2)–O(1)–Fe(3)	120.2 (1)	119.6 (2)
O(1)–Fe(1)–N(20)	178.1 (1)	178.0 (2)
O(1)–Fe(2)–N(30)	177.9 (1)	178.2 (2)
O(1)–Fe(3)–N(40)	178.7 (1)	177.3 (2)
Fe(1)–Fe(2)–Fe(3)	60.94	60.32
Fe(1)–Fe(3)–Fe(2)	59.31	59.52
Fe(2)–Fe(1)–Fe(3)	59.75	60.16

^a Average distance between metal and oxygen atoms of the acetate group.

a difference in orientation of molecular dipole moments of toluene compared to 3-Me-py.

Combination of the four structure determinations reported herein with three previously reported investigations provides additional insight into the charge distribution in these mixed-valence complexes. In Figure 11 drawings based on these seven determinations are presented along with a summary of Fe–O bond lengths. The first conclusion to be drawn from these drawings is that the preferred orientation for the pyridine ligands is staggered with respect to the Fe–acetate bonds. In all cases these ligands are very nearly parallel to or perpendicular to the Fe_3O plane. This gives rise to four possible isomers having 3, 2, 1, or 0 pyridine ligands in the Fe_3O plane; all four isomers are represented in the set of complexes in Figure 11.

With respect to the dynamics of intramolecular electron transfer, it should first be noted that the two asymmetric isomers are the species that give “localized” Mössbauer spectra at room temperature, while the species with symmetric conformations are those that exhibit a single doublet. While other effects may influence the electron-transfer rate, there can be little doubt that the ground-state conformation is the major determinant of the potential-energy surface for electron transfer. This observation also suggests that ligand dynamics could provide a driving force for electron transfer.

While the structural data give little direct insight into the dynamics of the electron transfer, information related to the relative energies of the potential-energy minima for the system can be obtained from an examination of the interatomic distances. The strong correlation between Fe–O(oxide) and Fe–O(acetate) distances observed in Figure 12 supports the hypothesis that these distances reflect the average oxidation state of the iron in a

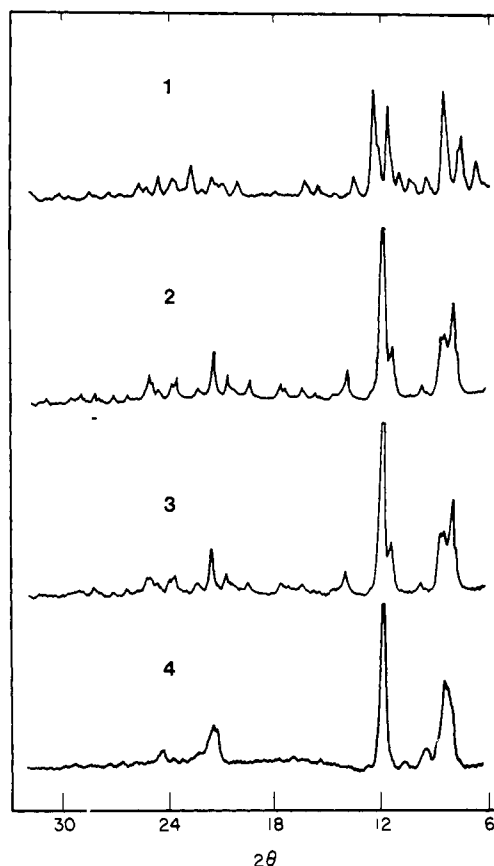


Figure 9. Room temperature X-ray powder diffraction patterns for (1) $[\text{Fe}_3\text{O}(\text{O}_2\text{CCH}_3)_6(3\text{-Me-py})_3](\text{CH}_3\text{CN})$, (2) $[\text{Fe}_3\text{O}(\text{O}_2\text{CCH}_3)_6(3\text{-Me-py})_3](\text{toluene})$, (3) $[\text{Fe}_3\text{O}(\text{O}_2\text{CCH}_3)_6(3\text{-Me-py})_3](3\text{-Me-py})$, and (4) $[\text{Fe}_3\text{O}(\text{O}_2\text{CCH}_3)_6(3\text{-Me-py})_3](\text{benzene})$.

particular crystallographic site. The very small scatter in Figure 12 is an indication of both the quality of the crystallographic data and the fact that these distances are relatively insensitive to “packing effects” (although in the case of the symmetric isomers any localization of charge must arise from interaction of the complex with its surroundings).

The Fe–O distances observed for the two asymmetric isomers provide further evidence that the orientations of the pyridine ligands influence the charge distribution. In the complex with a single ligand parallel to the Fe_3O plane, the unique iron atom has Fe–O distances substantially longer than those of the other two, suggesting that the “extra electron” resides primarily on the unique iron atom.

In the complex with two pyridine ligands in the Fe_3O plane, it again appears that the extra electron is associated with the in-plane ligands. In this case the unique iron atom (with its pyridine ligand perpendicular to the Fe_3O plane) has short Fe–O distances very similar to those observed for the “ferric” site in the other asymmetric isomer. The two iron atoms with in-plane pyridine ligands have Fe–O distances very close to the average of those for the “ferric” and “ferrous” sites in the other asymmetric isomer. These observations, taken with the fact that all of the isomeric species give low-temperature Mössbauer spectra with

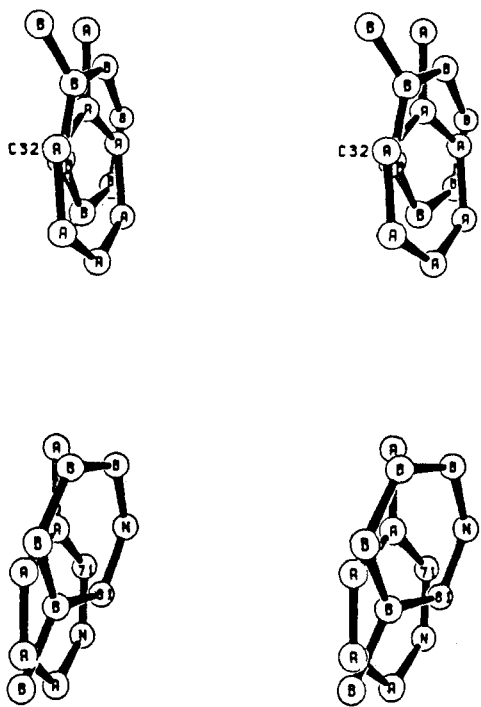


Figure 10. Stereoscopic views showing the two positions of the disordered solvate molecules in (top) $[\text{Fe}_3\text{O}(\text{O}_2\text{CCH}_3)_6(3\text{-Me-py})_3](\text{toluene})$ and (bottom) $[\text{Fe}_3\text{O}(\text{O}_2\text{CCH}_3)_6(3\text{-Me-py})_3](3\text{-Me-py})$.

“ferric” and “ferrous” signals in the ratio of 2:1, require that the crystallographic parameters be interpreted in terms of a disorder between two species, both of which have a localized ferrous iron atom associated with an in-plane pyridine ligand. It should be noted that in the case of the asymmetric isomer for which crystallographic data are available at two temperatures, the Fe–O distances become slightly more equivalent at high temperature, consistent with the population of states in which the ferrous ion is localized on the other two sites.

In view of the foregoing discussion, one might expect that for the symmetric isomers one would observe equivalent Fe–O distances for the three iron atoms, resulting from an unresolved disorder of three nearly degenerate states. Indeed for $[\text{Fe}_3\text{O}(\text{O}_2\text{CCH}_3)_6(\text{py})_3](\text{py})$ the molecule resides on a site of 32 crystallographic symmetry above 200 K. Below 200 K, however, there is a phase transformation that appears to involve loss of the threefold axis. Unfortunately crystal twinning has thus far precluded structure determination below this transition.

Rather surprisingly, the other symmetric isomers represented in Figure 11 exhibit quite asymmetric Fe–O distances both at low temperature where they give two-doublet Mössbauer spectra and at room temperature where the Mössbauer spectrum consists of a single doublet. In the case of the 3-Me-py solvate for which low-temperature crystallographic data are available, the observed Fe–O distances are very similar to those of the asymmetric CH_3CN solvate. Again the shortest distances appear to be almost completely “ferric” in character. The very similar pattern of Fe–O distances found in the independent room temperature structure determinations of the isostructural toluene and 3-Me-py solvates is noteworthy. In the absence of information available from heat-capacity measurements, the temperature dependence of the structure of the 3-Me-py complex would be difficult to interpret. While as expected the structure is somewhat more symmetric at higher temperature, and while both structures exhibit a pseudomirror symmetry, the orientations of the pseudomirrors are different at the two temperatures. This rather drastic temperature dependence is most likely associated with the two phase transitions observed in the heat-capacity measurements between the temperatures of the two structure determinations, although the detailed nature of these transitions is not obvious from the structural data.

Solid-State ^2H NMR Data. In Figure 13 are shown a series of powder ^2H NMR spectra obtained from **2** in which the toluene

solvate molecule is deuterated at the methyl group ($\text{C}_6\text{H}_5\text{CD}_3$). The room temperature spectral breadth of ~ 34 kHz is somewhat less than the breadth of ~ 41 kHz expected for a rotating methyl group and thus indicates that, in addition, the para axis of the toluene solvate molecule undergoes small amplitude dynamic reorientation. A sharp central feature is observed, most noticeably at high temperature, and likely arises from exchange broadening in which a dynamical rate, comparable to the quadrupolar coupling, cf. 10^{-3} s $>$ $\tau_c >$ 10^{-5} s, is present. The central feature is diminished as the temperature is lowered and the spectral breadth increases. These spectra are roughly symmetrical about the zero frequency for diamagnetic compounds and thus indicate that paramagnetic shifts are substantially smaller than the residual quadrupolar coupling. Quadrupolar splittings and paramagnetic shifts estimated from the apparent perpendicular edges of the powder patterns over the temperature range 153–293 K are shown in the inset of Figure 17. The quadrupolar splitting for this orientation approaches the value of ± 21 kHz expected for pure methyl group rotation at 153 K.

Spectra obtained from randomly and magnetically oriented⁴⁹ samples of **2** with perdeuterated solvate are shown in Figure 14. For several reasons, the powder spectra in Figure 14 are complicated and permit only simple analysis. The superimposed pattern arising from the methyl deuterons is readily seen for all temperatures above 153 K. The broader features are then due to the ring deuterons and, from the total pattern breadth, a maximum quadrupolar splitting of 68 kHz is observed at 298 K. Compared to the value of 140 kHz for rigid phenyl ring deuterons, large-amplitude dynamic reorientation of the solvate phenyl ring is consequently required. As the temperature is lowered, the maximum quadrupolar splittings increases to 80 kHz at 153 K. At 140 K (the lowest temperature accessible with the available equipment) there is a substantial change in pattern shape and the maximum splitting is about 85 kHz. The two doublets seen in spectra of the magnetically oriented powder sample, Figure 14, arise from the ortho and meta ring deuterons (outer doublet) and the methyl deuterons (inner doublet), as discussed below. The quadrupolar splitting for the methyl deuterons has a much smaller temperature dependence ($\Delta\nu_Q = 7$ kHz at 300 K and $\Delta\nu_Q = 8$ kHz at 144 K) than that for the ring deuterons ($\Delta\nu_Q = 36$ kHz at 300 K and $\Delta\nu_Q = 45$ kHz at 144 K). From the powder spectra we conclude that, at all temperatures examined in the NMR experiments, the toluene solvate is subject to large-amplitude dynamic disorder. For temperatures below 150 K, the para axis has a nearly fixed orientation but the phenyl ring is dynamic at even lower temperatures. Furthermore, ordering of the ring increases steadily as the temperature is lowered from 300 to 140 K, and presumably by the temperature of liquid nitrogen when most lattice contractions are complete, the motion of the toluene solvate molecules would stop. Thus, there is a good correspondence between the temperature range where the toluene solvate molecules experience an onset of motion and where Mössbauer data show the rate of electron transfer is increasing.

The details of the solvate dynamics at high temperatures were examined by single-crystal ^2H NMR. Shown in Figure 15 are spectra taken at 293 K from a three-axis rotation study of a single crystal (arbitrarily mounted) of **2** with perdeuterated toluene solvate. For most, but not all, orientations two well-resolved quadrupole-split doublets are observed. For some orientations, particularly those obtained from the x -axis rotation, the spectral line width is large and the signal-to-noise ratio low, again indicating possible exchange broadening. Rotation plots of the quadrupolar splitting as a function of goniometer angle are shown in Figure 16 and correspond to the expected 2θ periodicity. Fitting the data to a function of the expected form $(\pm\nu_{\text{obsd}} = +1/2(\langle V_{kk} \rangle + \langle V_{jj} \rangle) + 1/2(\langle V_{kk} \rangle - \langle V_{jj} \rangle) \cos 2\theta + \langle V_{jk} \rangle \sin 2\theta, i = x, y, z)$ is satisfactory except for the x -axis data ($\theta > 110^\circ$) where possible exchange was noted. Equivalent analyses of the paramagnetic shifts were also carried out. Experimental uncertainties are larger for the paramagnetic effects since the maximum shifts (~ 6 kHz)

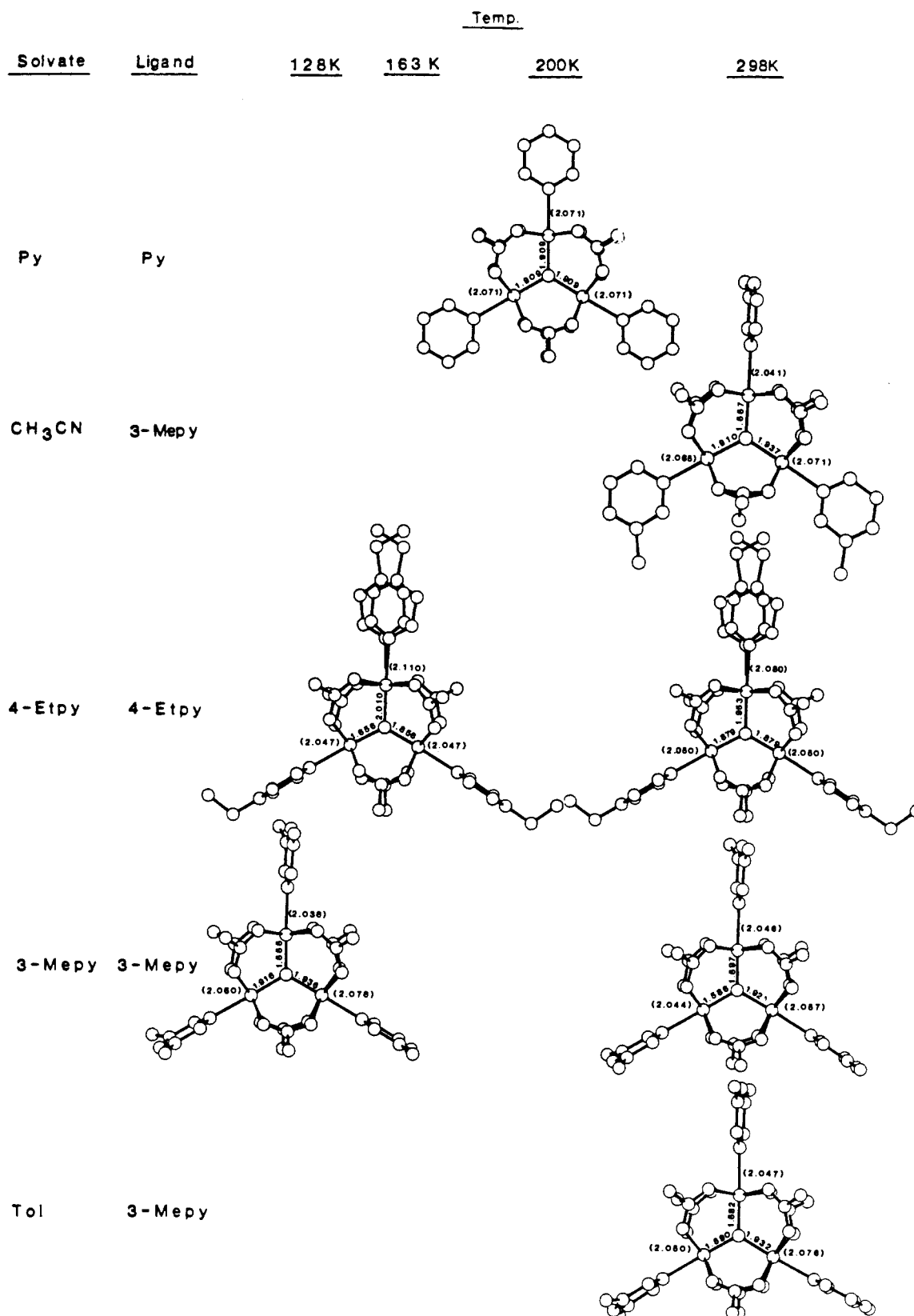


Figure 11. Summary of the molecular conformations and selected bond distances from the 7 X-ray structure determinations for 5 different μ_3 -oxo-bridged mixed-valence iron-acetate complexes.

are only several fold larger than the line widths. The residual quadrupolar, $\langle V_{ij} \rangle$, and paramagnetic, P_{ij} , tensor components and the principal values with corresponding Euler angles are listed in Table XIII. For the elements of a given quadrupolar tensor, the relative but not the absolute signs are determined in these experiments. The principal components of tensors listed in Table XIII are in accord with the powder spectra of Figures 13 and 14.

The tensors listed in Table XIII were first subjected to a rotation, $R_z(\Phi)R_y(\theta)$, with θ and Φ chosen to transform the components into the easy axis frame. For both a magnetically oriented powder and single-crystal samples, equivalent doublet frequencies were observed (-42.4, -13.5, 0.4, and 30.2 kHz). Rotation of the oriented single-crystal sample assigned the inner doublet (-13.5 and 0.4 kHz) for this particular orientation to the methyl deu-

Table XIII. Residual Quadrupolar Coupling and Paramagnetic Tensor Components in Various Reference Frames^a

label position	tensor	frame	T_{xx} (kHz)	T_{yy} (kHz)	T_{zz} (kHz)	T_{xy} (kHz) [or α (deg)]	T_{xz} (kHz) [or β (deg)]	T_{yz} (kHz) [or γ (deg)]
methyl	(V)	easy axis	± 2.0	∓ 8.9	± 6.8	∓ 9.4	∓ 23.6	± 6.8
methyl	(V)	PAS	± 11.4	∓ 20.0	± 31.3	[58]	[45]	[22]
ring	(V)	easy axis	± 24.3	∓ 59.5	± 36.3	∓ 27.9	± 32.5	∓ 5.0
ring	(V)	PAS	∓ 68.1	± 67.2	± 2.1	[-4]	[47]	[21]
ring	(V)	PAS (methyl)	± 39.2	∓ 40.1	± 2.1	∓ 54.7	± 0.9	∓ 2.4
methyl	P	easy axis	3.4	-0.5	-5.5	-0.3	-0.1	1.3
methyl	P	PAS	3.4	-0.2	-5.8	[95]	[13]	[-90]
ring	P	easy axis	1.8	1.5	-6.4	1.9	-0.5	-0.8
ring	P	PAS	3.7	-0.3	-6.5	[-158]	[6]	[116]

^aEntries for the off-diagonal components of principal axis system (PAS) tensors are the Euler angles (α, β, γ) relative to the easy axis frame. Uncertainties in the component values are ± 1.5 kHz and $\pm 4^\circ$ in the Euler angles.

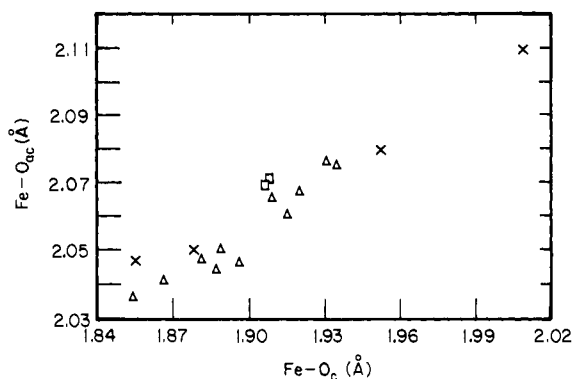


Figure 12. Correlation of Fe-O_{ac}(acetate) vs. Fe-O_c(oxide) distances from the structural data summarized in Figure 11.

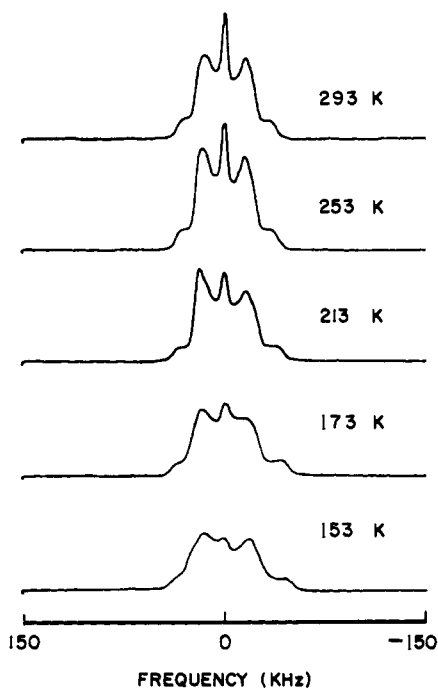


Figure 13. Variable-temperature powder ²H NMR spectra for the toluene solvate $[\text{Fe}_3\text{O}(\text{O}_2\text{CCH}_3)_6(3\text{-Me-py})_3](\text{C}_6\text{H}_5\text{CD}_3)$.

terons. By computer search, a unique choice of $(\Phi, \theta) = (5 \pm 4^\circ, 68 \pm 2^\circ)$ was found. From rotation studies of magnetically oriented powder samples frozen in paraffin we know these samples to be essentially randomly oriented about the easy axis, which for the related cluster, $[\text{Fe}_3\text{O}(\text{O}_2\text{CCH}_3)_6(\text{py})_3] \cdot (\text{py})$, is normal to the Fe_3O plane.³⁴ Thus, the tensor components listed in Table XIII have a well-defined orientation with respect to the cluster normal (specified by the Euler angles α and β) but an unknown crystallographic orientation in the perpendicular plane (specified by γ). The angle γ serves only for comparison of the relative orientations of the component values listed in Table XIII.

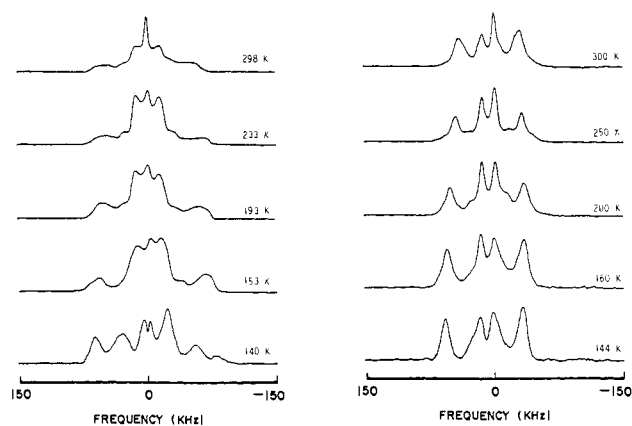


Figure 14. Variable-temperature powder ²H NMR spectra for the toluene solvate $[\text{Fe}_3\text{O}(\text{O}_2\text{CCH}_3)_6(3\text{-Me-py})_3](\text{C}_6\text{D}_5\text{CD}_3)$. The spectra on the left-hand side are for a sample which is randomly oriented and the spectra on the right-hand side are for a sample which is magnetically oriented.

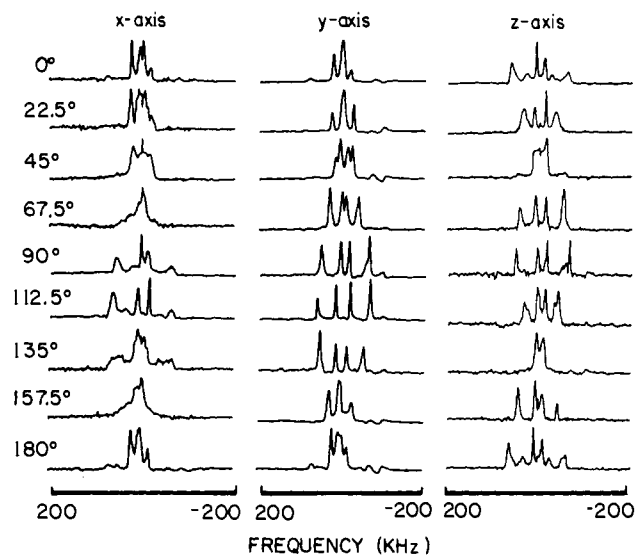


Figure 15. ²H NMR spectra obtained for a $1 \times 1 \times 1$ mm single crystal of $[\text{Fe}_3\text{O}(\text{O}_2\text{CCH}_3)_6(3\text{-Me-py})_3](\text{C}_6\text{D}_5\text{CD}_3)$ at 293 K. Spectra are presented for rotation of the single crystal about three mutually orthogonal axes.

Straightforward matrix analysis shows that the dihedral angles, ψ_{iz} , between principal component T_{ii} and the easy axis are given by

$$\psi_{xz} = \cos^{-1}(\sin \beta \cos \alpha)$$

$$\psi_{yz} = \cos^{-1}(\sin \beta \sin \alpha)$$

$$\psi_{zz} = \beta$$

and, as expected, are well-defined in the molecular frame since they depend only on α and β .

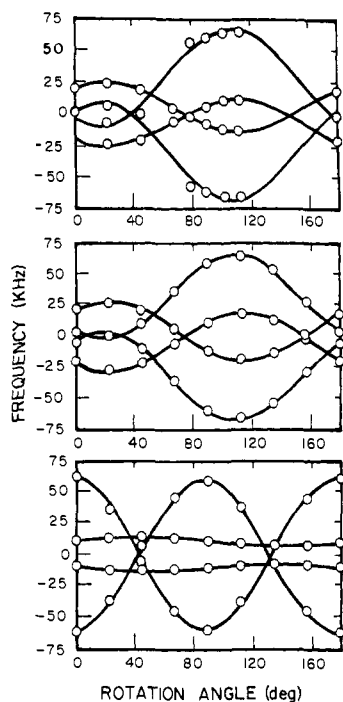


Figure 16. Rotation plots of the quadrupolar splitting as a function of goniometer angle for the two quadrupole-split doublets seen in the ^2H NMR spectra (see Figure 15) for a single crystal of $[\text{Fe}_3\text{O}(\text{O}_2\text{CCH}_3)_6(3\text{-Me-py})_3](\text{C}_6\text{D}_5\text{CD}_3)$. Data obtained from the x -axis mounting are shown on top, y -axis data in the middle plot, and the z -axis data in the bottom plot.

The tensor components (V_{ij}) and P_{ij} for the doublet with smaller maximum quadrupolar splitting are readily assigned to the three equivalent toluene methyl deuterons. These tensor components were used to calculate a powder pattern (see Appendix B) which, as shown in Figure 17, superimposes nearly identically over the experimental powder pattern obtained at the same temperature (293 K) with the exception of the previously noted central feature. The other doublet, which has a somewhat larger intensity, is then assigned to the four ortho and meta deuterons of the solvate ring. The para deuteron, not subject to the averaging of the methyl group about the para axis, would be expected to have principal components of the quadrupolar tensor roughly coaxial to those of the methyl group but ~ 3 times larger. Such a large coupling is not observed, presumably due to the fact that this doublet would be less than (due to limited excitation bandwidth) $1/4$ the intensity of the ring deuteron doublet. Also, due to its relative rigidity, T_1 will be long resulting in additional attenuation due to saturation.

The paramagnetic tensors for the ring and methyl deuterons have similar principal values, the component of largest magnitude is along the easy axis, and the tensors are substantially nonaxial. Compared to the approximately axial tensor for the complex $[\text{Fe}_3\text{O}(\text{O}_2\text{CCH}_3)_6(4\text{-Me-py})_3]\cdot\text{C}_6\text{D}_6$, where the solvate is sandwiched between two stacked clusters,³⁴ the principal components of the tensors observed in this study are a factor of ~ 3 smaller and for a sample aligned along the easy axis the shifts are of opposite sign. These results are consistent with the X-ray structure. The cluster-solvate distance in **2** is larger than that in $[\text{Fe}_3\text{O}(\text{O}_2\text{CCH}_3)_6(4\text{-Me-py})_3]\cdot\text{C}_6\text{D}_6$, and the nearest-neighbor cluster-solvate vectors are perpendicular rather than parallel to the easy axis (principal component of the susceptibility tensor). For iron cluster systems, the \mathbf{g} tensors have small anisotropies, consequently the coupling between a single cluster and the nuclear spin is approximately axially symmetric about the cluster-nuclear spin vector. The near axially of the \mathbf{P} tensor for $[\text{Fe}_3\text{O}(\text{O}_2\text{CCH}_3)_6(4\text{-Me-py})_3]\cdot\text{C}_6\text{D}_6$ results since the vectors for the two nearest clusters, above and below the solvate, are parallel. As described above, the structure of the complex $[\text{Fe}_3\text{O}(\text{O}_2\text{CCH}_3)_6(3\text{-Me-py})_3]\cdot\text{toluene}$ shows three nearest neighbors and the nonaxiality of the \mathbf{P} tensors arises since the three nearest-

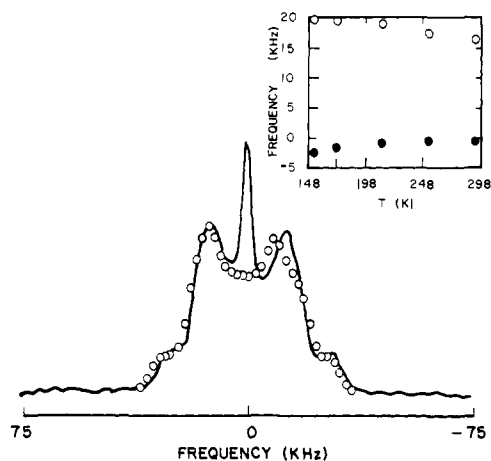


Figure 17. ^2H NMR spectrum taken at 293 K for a powder sample of $[\text{Fe}_3\text{O}(\text{O}_2\text{CCH}_3)_6(3\text{-Me-py})_3](\text{C}_6\text{H}_5\text{CD}_3)$. The solid line represents the experimental spectrum, whereas the circles represent a simulated powder pattern obtained by using the quadrupolar coupling and paramagnetic shift tensor components from an analysis of the spectra obtained for the single crystal of $[\text{Fe}_3\text{O}(\text{O}_2\text{CCH}_3)_6(3\text{-Me-py})_3](\text{C}_6\text{D}_5\text{CD}_3)$.

neighbor cluster-solvate vectors are not parallel. Furthermore, the paramagnetic tensors are not traceless. This could arise from experimental inaccuracies (the traces are only slightly larger than experimental inaccuracies of $\sim \pm 1.5$ kHz), a small anisotropy in the cluster \mathbf{g} tensor (necessary since the samples orient in the magnetic field), or a small contact interaction between the solvate and cluster.

Of particular interest is that the four ortho and meta ring deuterons yield a single doublet for the general orientation. For aromatic deuterons, the static quadrupolar coupling tensor is, to a good approximation, axially symmetric about the C-D bond with a coupling along this axis of 140 kHz. That is, assuming no dynamical averaging, the ortho and meta deuterons would be expected for the general orientation to give two resolved doublets: one arising from the coaxial C-D groups at ring positions 2 and 5 and a second doublet from positions 3 and 6. Since a single doublet is observed, the phenyl ring dynamics are such that deuterons 2 and 6 (and 3 and 5) are equivalent.

A simple process for making the ring deuterons equivalent is a twofold ring flip about the para axis which interchanges deuterons 2 and 6 (and deuterons 3 and 5). All four deuterons will then display equivalent coupling tensors with residual principal components of $-1/2\nu_Q = -70$ kHz along the ring normal, $-1/8\nu_Q = -17$ kHz along the para axis, and $5/8\nu_Q = 87$ kHz along the mutually orthogonal axis. Such a process has been experimentally observed in powder ^2H NMR spectra of tyrosine phenyl rings of small peptides.⁵⁰

The residual principal quadrupolar coupling tensor components observed for both the methyl and ring deuterons are qualitatively similar to but quantitatively less than expected from simple model considerations, cf. threefold (or higher) rotation of the methyl and twofold jump rotation of the ring about a stationary para axis. Also, the ring deuteron tensor, as shown in Table XIII, is only block diagonal rather than diagonal in the principal axis frame of the methyl deuteron tensor as expected for the simple model. The large component of the methyl tensor is coincident with the small component of the ring tensor; as expected, however, the remaining components of the two tensors are not. A perturbation approach for quantitatively analyzing these results is presented in Appendix A. The model described above is taken as the zero-order picture, and the additional dynamics, the perturbation, appear as averages linear (first-order effects) and quadratic (second-order effects) in Euler angles. The averages contained in the analysis are $\langle\beta^2\rangle - \langle\beta\rangle^2$, $\langle(\alpha + \gamma)^2\rangle$, and $\langle\alpha + \gamma\rangle$. They

(50) Rice, D. M.; Wittebort, R. J.; Griffin, R. G.; Meirovitch, E.; Stinson, E. R.; Meinwald, Y. C.; Scheraga, H.; Freed, J. H. *J. Am. Chem. Soc.* **1981**, *103*, 7707.

Table XIV. Dynamical Constants and Average Orientation of the Solvate in $[\text{Fe}_3\text{O}(\text{O}_2\text{CCH}_3)_6(3\text{-Me-py})_3]\cdot\text{toluene}$ from X-ray Structural Analysis and ^2H NMR^a

method	comment	$\Delta\beta$, deg	$\Delta(\alpha + \gamma)$	$(\alpha + \gamma)$	$\langle\psi_{xz}\rangle$	$\langle\psi_{zz}\rangle$
^2H NMR	from Me label	22				$45 \pm 4^\circ$
^2H NMR	from ring label	22	8°	20°	$43 \pm 4^\circ$	$45 \pm 4^\circ$
X-ray	<i>b</i>	22	3°	10°	44°	51°

^a $\langle\psi_{iz}\rangle$ is the average dihedral angle between the *i*th coordinate, as defined in Appendix A, of the solvate and the easy axis. Thus $\langle\psi_{yz}\rangle$ and $\langle\psi_{zz}\rangle$ are the average dihedral angles for the solvate ring normal and para axes, respectively. $\Delta\Omega = ((\Omega^2) - (\Omega')^2)^{1/2}$ with $\Omega = \beta$ and $(\alpha + \gamma)$. ^b From the X-ray analysis two sets of Euler angles, $(\alpha, \beta, \gamma) = (-59^\circ, 51^\circ, 66^\circ)$ and $(-70^\circ, 51^\circ, 66^\circ)$ relative to a Cartesian frame with the *z* axis perpendicular to the cluster plane were determined from the coordinates.

are small-angle expansions of order parameters but have a more obvious physical meaning. $\Delta\beta = ((\beta^2) - (\beta')^2)^{1/2}$ and $\Delta(\alpha + \gamma) = (((\alpha + \gamma)^2) - (\alpha + \gamma')^2)^{1/2}$ are the standard deviations of the *z*-axis fluctuation and rotation about that axis, respectively, and $(\alpha + \gamma)$ is the average rotation about the *z* axis. Furthermore, the *x*, *y*, and *z* axes are, in effect, labeled by the residual principal components. For example, an axially symmetric coupling tensor with its unique axis along a C–D bond subjected to a fast averaging process also of axial symmetry yields an averaged tensor of axial symmetry with the unique axis along the average orientation of the original tensor. Thus, determining the orientation of the residual tensor in a crystallographic lattice in turn determines the average orientation of the C–D bond. In Appendix A the analogous problem for nonaxial tensors, both before and after averaging, is dealt with. It is shown to second order that the principal components of the averaged coupling tensor lie along the average positions of the *x*, *y*, and *z* axes. Simply stated, the orientation of the residual ^2H coupling tensor is equivalent to the average orientation of the toluene molecule.

The dynamical constants and average dihedral angles, computed from the ^2H NMR quadrupolar coupling data of Table XIII by using the analysis of Appendix A, are collected in Table XIV. Also included are the same parameters computed from the X-ray analysis where the coordinates of the two lattice positions of the toluene solvate molecule are used. The average dihedral angles, $\langle\psi_{iz}\rangle$, and the standard deviations, $\Delta\beta$ and $\Delta(\alpha + \gamma)$, are determined by the two methods to be in satisfactory agreement. In order to determine the coordinate, *i* = *x*, *y*, or *z* to which a dihedral angle $\langle\psi_{iz}\rangle$ is referenced, the corresponding residual principal components of the ring deuteron coupling tensor were labeled so that the values of $\Delta\beta$ determined from both the methyl and ring deuterons are equivalent within experimental error. Since $\Delta\beta$ is determined unambiguously to be 22° from the methyl data, this required the residual principal components for the ring to be 68.1, -67.2 , and -2.0 kHz for $\langle V_{xx}^{\text{PAS}} \rangle$, $\langle V_{yy}^{\text{PAS}} \rangle$, and $\langle V_{zz}^{\text{PAS}} \rangle$, respectively.

We note that the X-ray and NMR results are brought into close agreement with the finding that, in addition to small amplitude dynamics, the solvate phenyl ring undergoes twofold flips about its para axis, a local symmetry operation and thus not observed by X-ray analysis. Furthermore, the twofold flip persists even down to 140 K.

Summary and Comments

In the series $[\text{Fe}_3\text{O}(\text{O}_2\text{CCH}_3)_6(3\text{-Me-py})_3]\cdot\text{S}$ it was found that the solvate molecule S can have a pronounced effect on the rate of intramolecular electron transfer. On the one hand, changing the solvate molecule can lead to changes in the solid-state packing arrangement and the molecular conformation. In the S = CH_3CN complex, the solid-state environment about a given Fe_3O complex is not symmetric as a result of a "dimeric" association of two Fe_3O complexes. In this material the complex adapts an asymmetric conformation with two pyridine ligands nearly parallel to the Fe_3O plane and the third nearly perpendicular to this plane. The CH_3CN solvate exhibits a "valence-trapped" Mössbauer spectrum at room temperature. For the toluene and 3-Me-py solvates the solid-state environment about a given Fe_3O complex approximates to threefold symmetry and the complex adopts a symmetric conformation. In the case of these two complexes valence de-trapping on the Mössbauer time scale is seen as the sample temperature is increased.

The second way in which a solvate molecule can effect the rate of intramolecular electron transfer in a nearby Fe_3O complex is a reflection of the lattice cavity in which the solvate molecule is contained. If, as the temperature of the crystal is increased, the solvate molecule begins to move between different lattice positions, this will have an impact on the rate of electron transfer in the neighboring Fe_3O complexes. This motion in the solvate molecules about a given Fe_3O complex micro-modulates the outer-sphere coordination and may induce intramolecular electron transfer. For **2**, the onset of electron delocalization occurs at ~ 100 K and the ^2H NMR results, which extend down to 140 K, show the toluene solvate molecules are undergoing considerably less dynamical motion at 140 K than they are at 298 K.

In the PKS vibronic model⁵¹ for the electronic structure of mixed-valence complexes or in terms of theoretical models⁴⁴⁻⁴⁷ for mixed-valence Fe_3O -acetate complexes there are three factors that determine the nature of the ground-state potential-energy surface for a mixed-valence Fe_3O complex. The three factors are (1) the magnitude of electronic coupling between the d-orbitals on neighboring iron ions, (2) the magnitude of vibronic coupling between the vibrational distortion mode important in the electron transfer and the electronic coordinates, and (3) the zero-point energy differences between different vibronic states of the complex. There is no reason to expect the first two of these three factors to change as the solvate molecule is changed in $[\text{Fe}_3\text{O}(\text{O}_2\text{CCH}_3)_6(3\text{-Me-py})_3]\cdot\text{S}$. A change of the solvate molecule or in the nature (static or dynamic) of the solvate molecule likely changes the zero-point energy differences between the different vibronic states of the mixed-valence Fe_3O complexes. Such a change in the relative zero-point energy differences of the vibronic states of a Fe_3O complex will change the rate of intramolecular electron transfer in that Fe_3O complex no matter whether the electron transfer occurs via thermal activation over the barrier or by electron and nuclear tunneling through the barrier.

There could be similar phenomena occurring in thermochromic,⁴⁻⁸ Jahn–Teller distorted,^{16,24} and spin-crossover²⁵⁻³⁰ complexes. For example, in the case of the spin-crossover complex $[\text{Fe}(2\text{-pic})_3]\text{Cl}_2\cdot\text{solvate}$ (solvate = ethanol or methanol) it could be that it is the onset of lattice dynamics on the part of the solvate molecules which triggers off the relatively abrupt conversion of the sample from low spin to high spin as the temperature of the compound is increased. The lattice with the dynamical solvate molecules is softer and this tends to stabilize the high-spin state compared to the situation where the solvate molecules are statically hydrogen bonded to the spin-crossover complexes.

Acknowledgment. We are grateful for support from National Institutes of Health Grants HL13652 (D.N.H.) and GM35329 (C.E.S.) and from National Science Foundation Grants PCM-8118912 (R.J.W.) and CHE-8340836 (C.E.S.).

Appendix A

We show here a perturbation method for analyzing the residual ^2H quadrupolar coupling tensors determined for the toluene methyl and ring deuterons. For the zero-order tensors we assume the

(51) Wong, K. Y.; Schatz, P. N. *Prog. Inorg. Chem.* **1981**, 28, 369.

(52) Rao, C. N. R.; Rao, K. J. *Phase Transitions in Solids*; McGraw-Hill: New York, 1978.

(53) Mehring, M. *High Resolution NMR in Solids*; Springer-Verlag: New York, 1983.

methyl group undergoes fast reorientation about the para axis with at least threefold symmetry and the ring undergoes twofold jumps about this same axis. The resulting quasistatic tensors, in a coordinate frame with *z* along the para axis, *y* normal to the ring plane, and *x* orthogonal to *y* and *z*, are

$$\mathbf{V} = \frac{\nu_q}{6} \begin{pmatrix} -1 & 0 & 0 \\ 0 & -1 & 0 \\ 0 & 0 & 2 \end{pmatrix} \quad (\text{A1a})$$

for the methyl group and

$$\mathbf{V} = \frac{\nu_q}{2} \begin{pmatrix} 5/4 & 0 & 0 \\ 0 & -0 & 0 \\ 0 & 0 & -1/4 \end{pmatrix} \quad (\text{A1b})$$

for the ortho and meta ring deuterons. The coupling tensors averaged over the additional fluctuation, treated as a perturbation, are computed as

$$\langle \mathbf{V} \rangle = \langle \delta(\alpha, \beta, \gamma) \mathbf{V} \delta^\dagger(\alpha, \beta, \gamma) \rangle \quad (\text{A2})$$

where the average is over Euler angles and $\delta(\alpha, \beta, \gamma) = \delta(\alpha + \gamma, \beta)$ is the usual orthogonal rotation matrix, \mathbf{R} , expanded to second order (satisfactory for $|\alpha + \gamma|$ and $|\beta| < \sim 30^\circ$).

$$\mathbf{R}(\alpha, \beta, \gamma) = \delta(\alpha + \gamma, \beta) =$$

$$\begin{pmatrix} [1 - \beta^2/2 - (\alpha + \gamma)^2/2] & [\alpha + \gamma] & -\beta \\ -[\alpha + \gamma] & [1 - (\alpha + \gamma)^2/2] & 0 \\ \beta & 0 & [1 - \beta^2/2] \end{pmatrix} \quad (\text{A3})$$

As in all following calculations, off-diagonal elements are only retained to first order, since higher order off-diagonal elements have no effect on eigenvalues and eigenvectors calculated to second order. The averaged coupling tensors are

$$\langle \mathbf{V} \rangle = \frac{\nu_q}{6} \begin{pmatrix} [-1 + 3\langle \beta^2 \rangle] & 0 & -\langle \beta \rangle \\ 0 & -1 & 0 \\ -\langle \beta \rangle & 0 & [2 - 3\langle \beta^2 \rangle] \end{pmatrix} \quad (\text{A4a})$$

for the methyl deuterons and

$$\langle \mathbf{V} \rangle = \frac{\nu_q}{2} \times \begin{pmatrix} [5/4 - 3/2 \langle \beta^2 \rangle - 9/4 \langle (\alpha + \gamma)^2 \rangle] & -9/4 \langle \alpha + \gamma \rangle & 3/2 \langle \beta \rangle \\ -9/4 \langle \alpha + \gamma \rangle & [-1 + 9/4 \langle (\alpha + \gamma)^2 \rangle] & 0 \\ 3/2 \langle \beta \rangle & 0 & [-1/4 + 3/2 \langle \beta^2 \rangle] \end{pmatrix} \quad (\text{A4b})$$

for the ring deuterons. The tensor, eq A4a, is diagonalized according to the following eigenvalue problem

$$\langle \mathbf{V} \rangle \delta(0, \langle \beta \rangle) = (\mathbf{V}^{\text{PAS}}) \delta(0, \langle \beta \rangle) \quad (\text{A5a})$$

with eigenvalues (residual principal components)

$$\langle V_{xx}^{\text{PAS}} \rangle = \frac{-\nu_q}{6} [1 - 3\langle \beta^2 \rangle - \langle \beta \rangle^2] \quad (\text{A5b})$$

$$\langle V_{yy}^{\text{PAS}} \rangle = \frac{-\nu_q}{6} \quad (\text{A5c})$$

$$\langle V_{zz}^{\text{PAS}} \rangle = \frac{\nu_q}{6} [2 - 3(\langle \beta^2 \rangle - \langle \beta \rangle^2)] \quad (\text{A5d})$$

The eigenvalues are labeled according to their unperturbed values, and the eigenvectors are found to be the corresponding columns of the rotation matrix, δ , evaluated at $(0, \langle \beta \rangle)$. There is no dependence on $(\alpha + \gamma)$ since the zero-order coupling tensor is axial.

Similarly, the ring deuteron tensor, eq A4b, is diagonalized according to

$$(\mathbf{V}) \delta(\langle \alpha + \gamma \rangle, \langle \beta \rangle) = (\mathbf{V}^{\text{PAS}}) \delta(\langle \alpha + \gamma \rangle, \langle \beta \rangle) \quad (\text{A6a})$$

with eigenvalues

$$\langle V_{xx}^{\text{PAS}} \rangle = \frac{\nu_q}{2} \left[\frac{5}{4} - \frac{3}{2} (\langle \beta^2 \rangle - \langle \beta \rangle^2) - \frac{9}{4} (\langle (\alpha + \gamma)^2 \rangle - \langle \alpha + \gamma \rangle^2) \right] \quad (\text{A6b})$$

$$\langle V_{yy}^{\text{PAS}} \rangle = \frac{\nu_q}{2} \left[-1 + \frac{9}{4} (\langle (\alpha + \gamma)^2 \rangle - \langle \alpha + \gamma \rangle^2) \right] \quad (\text{A6c})$$

$$\langle V_{zz}^{\text{PAS}} \rangle = \frac{\nu_q}{2} \left[-\frac{1}{4} + \frac{3}{2} (\langle \beta^2 \rangle - \langle \beta \rangle^2) \right] \quad (\text{A6d})$$

Comparison of the experimental principal components of the methyl and ring deuteron tensors with eq 5 and 6 allows one to evaluate the standard deviations $[\langle \beta^2 \rangle - \langle \beta \rangle^2]^{1/2}$ and $[\langle (\alpha + \gamma)^2 \rangle - \langle \alpha + \gamma \rangle^2]^{1/2}$.

Equation A6a shows that the ring deuteron principal components lie along the axes of a coordinate system with orientation $(\langle \alpha + \gamma \rangle, \langle \beta \rangle)$, i.e., the average orientation. Consequently we conclude, in the context of our second-order analysis, that the eigenvectors of the ring deuteron tensor in a chosen reference frame determine the average orientation of the toluene molecule in that frame. This result is general to any non-axial tensor subject to small-amplitude motions and leads to an unambiguous orientation insofar as the averaged principal components can be correlated with their corresponding zero-order values.

The methyl and ring deuteron tensors have a fixed relative orientation, a fact which can be utilized to determine $\langle \alpha + \gamma \rangle$. Since the "z column" of δ depends only on (β) , $\langle V_{zz}^{\text{PAS}} \rangle$ for both labels lie along the same axis. This results strictly from the assumption of small-amplitude motions. A full comparison of the two tensors is then facilitated by block diagonalizing one tensor in the principal axis frame of the other. The (*x, y*) block of the ring tensor, of A4b, transformed into the methyl principal axis frame is

$$\delta^\dagger(0, \langle \beta \rangle) \langle \mathbf{V} \rangle \delta(0, \langle \beta \rangle) = \frac{\nu_q}{2} \times \begin{pmatrix} [5/4 - 3/2 \langle (\beta^2) - \langle \beta \rangle^2 \rangle - 9/4 \langle (\alpha + \gamma)^2 \rangle] & -9/4 \langle \alpha + \gamma \rangle \\ -9/4 \langle \alpha + \gamma \rangle & [-1 + 9/4 \langle (\alpha + \gamma)^2 \rangle] \end{pmatrix} \quad (\text{A7})$$

which allows determination of $\langle \alpha + \gamma \rangle$ and thus $\langle (\alpha + \gamma)^2 \rangle$ as well when compared with the experimental tensor.

Appendix B

Powder patterns were computed directly from the quadrupolar, (V_{ij}), and paramagnetic tensor components, P_{ij} , determined by single-crystal studies as follows: Using standard methods,⁵³ the doublet resonance frequencies, ν_0 , for a given crystal orientation (α, β) are

$$\nu_0(\alpha, \beta) = \pm \nu_q + \nu_p \quad (\text{B1})$$

where

$$\begin{aligned} \nu_i = & \frac{1}{3} \text{Tr}(\mathbf{T}) + \frac{1}{2} \sin^2 \beta [(T_{xx} - T_{yy}) \cos 2\alpha - 2T_{xy} \sin 2\alpha] \\ & - \sqrt{2} \sin \beta \cos \beta [T_{xz} \cos \alpha - T_{yz} \sin \alpha] \\ & + \frac{1}{2} (3 \cos^2 \beta - 1) \left(T_{zz} - \frac{1}{3} \text{Tr}(\mathbf{T}) \right) \end{aligned} \quad (\text{B2})$$

i = q, p and $T_{ij} = \langle V_{ij} \rangle, P_{ij}$, respectively.

The pattern was then computed as a sum of Gaussian line shapes, $\exp[-(\nu - \nu_0(\alpha, \beta))^2/2\Delta^2]$, with line width Δ . For computational efficiency, the Gaussian doublets for a given orientation were truncated at $\nu_0(\alpha, \beta) \pm 3\Delta$. The sum over orientations was

computed by using equal area elements on the sphere. This was done with equal increments in β (typically 0.5°) and variable increments in α proportional to $\sin \beta$.

Supplementary Material Available: Tables of calculated hy-

drogen atom coordinates, anisotropic and isotropic thermal parameters, and bond distances and angles for the X-ray structures of **1** to 298 K, **2** at 298 K, and **3** at 128 and 298 K (27 pages); listing of structure factor amplitudes (79 pages). Ordering information is given on any current masthead page.

Protein Structure and Interactions by Combined Use of Sequential NMR Assignments and Isotope Labeling

Hans Senn,[†] Gottfried Otting, and Kurt Wüthrich*

Contribution from the Institut für Molekularbiologie und Biophysik, Eidgenössische Technische Hochschule, CH-8093 Zürich-Hönggerberg, Switzerland. Received August 22, 1986

Abstract: The 10 leucyl residues in the DNA-binding domain consisting of the 76 N-terminal residues of *Salmonella* phage P22 c2 repressor were labeled with ^{15}N . By use of a novel $^{15}\text{N}(\omega_2)$ half-filter technique, simplified two-dimensional nuclear Overhauser enhancement spectra were obtained, which contain exclusively resonance peaks relating to at least one ^{15}N -bound hydrogen atom. Observation of nuclear Overhauser effects in these edited subspectra greatly facilitated sequential resonance assignments leading to sequence-specific assignments for all 10 leucines. Further potentialities of the combined use of residue-selective isotope labeling and sequential assignment procedures for studies of protein conformation in solution and for investigations of intermolecular interactions with proteins are discussed.

Nuclear magnetic resonance (NMR) is presently the only technique besides diffraction methods with single crystals that can be employed for three-dimensional structure determination with biopolymers.¹ With regard to studies of structure-function correlations in proteins and nucleic acids the significance of this new approach lies in the fact that NMR studies can be performed in aqueous solution or in other environments which may closely mimic the physiological milieu. Structure determination by NMR relies on one's ability to obtain sequence-specific ^1H NMR assignments.^{1,2} For small proteins these can efficiently be obtained by the sequential assignment technique.^{1,3,4} An alternative, straightforward approach for NMR assignments is by site-specific labeling with ^{13}C or ^{15}N ,^{1,5-8} which has, however, for practical reasons been used only on a limited scope. The present paper illustrates the potentialities of the combined use of sequential assignments and residue-specific isotope labeling with proteins. This approach enables NMR applications with more complex macromolecular systems and opens new avenues for studies of spatial structure and of intermolecular interactions.

Materials and Methods

For the experiments in this paper we used the DNA-binding domain consisting of the 76 N-terminal residues of *Salmonella* phage P22 c2 repressor, which was previously shown to retain the ability of the intact repressor protein for specific binding to DNA.^{9,10} c2 repressor 1-76 contains 10 Leu residues, which were all labeled with ^{15}N in the extent of >85%.¹¹

NMR spectra were recorded with a Bruker AM-360 spectrometer. For studies of the $[2-^{15}\text{N}]\text{Leu}$ c2 repressor 1-76 a new $^{15}\text{N}(\omega_2)$ half-filter experiment was introduced,¹² which is related to a previously described heteronuclear zero-quantum filter procedure.¹³ A two-dimensional ^1H nuclear Overhauser enhancement (NOESY) spectrum with a $^{15}\text{N}(\omega_2)$ half-filter was obtained by using the pulse sequence $90^\circ(^1\text{H})-t_1-90^\circ(^1\text{H})-\tau_m-90^\circ(^1\text{H})-\tau/2-180^\circ(^1\text{H},^{15}\text{N})-\tau/2-[180^\circ(^{15}\text{N})]$ acquisition. The editing $180^\circ(^{15}\text{N})$ pulse shown in brackets is applied in every second scan, and the difference of the spectra recorded with and without the editing pulse is taken. This experiment selects for the resonances of ^{15}N -bound amide protons along ω_2 but does not discriminate along ω_1 , thus providing dramatically simplified ^1H NOESY spectra with a high content of structural information.

Sequence-specific assignments for the ^{15}N -labeled amino acid residues were obtained with the usual sequential assignment procedures,¹⁻⁴ as is described in more detail in the following section.

Results and Discussion

Figure 1 shows different regions of a ^1H NOESY spectrum recorded with a $^{15}\text{N}(\omega_2)$ half-filter. On the diagonal from the upper right to the lower left there are exclusively the peaks of the ^{15}N -bound protons, which are split into four components by the one-bond ^{15}N - ^1H scalar coupling of ca. 90 Hz (Figure 1A). Nuclear Overhauser effects (NOE) between different ^{15}N -bound protons give rise to pairs of cross peaks symmetrically arranged with respect to this diagonal, which are split into four components by one-bond ^{15}N - ^1H scalar couplings along both ω_1 and ω_2 . Figure 1A contains two such cross peaks between different ^{15}N -labeled leucines. Finally, there are all the NOEs between leucine amide protons and protons not bound to ^{15}N . The corresponding NOESY cross peaks consist of two fine structure components separated by the ^{15}N - ^1H scalar coupling along ω_2 , and they are observed

(1) Wüthrich, K. *NMR of Proteins and Nucleic Acids*; Wiley: New York, 1986.

(2) Wüthrich, K.; Wider, G.; Wagner, G.; Braun, W. *J. Mol. Biol.* **1982**, *155*, 311-319.

(3) Billeter, M.; Braun, W.; Wüthrich, K. *J. Mol. Biol.* **1982**, *155*, 321-346.

(4) Wagner, G.; Wüthrich, K. *J. Mol. Biol.* **1982**, *155*, 347-366.

(5) Le Master, D. M.; Richards, F. M. *Biochemistry* **1985**, *24*, 7263-7269.

(6) Griffey, R. H.; Redfield, A. G.; Loomis, R. E.; Dahlquist, F. W. *Biochemistry* **1985**, *24*, 817-822.

(7) Live, D. H.; Davis, D. G.; Agosta, W. C.; Cowburn, D. *J. Am. Chem. Soc.* **1984**, *106*, 6104-6105.

(8) Weiss, M. A.; Redfield, A. G.; Griffey, R. H. *Proc. Natl. Acad. Sci. U.S.A.* **1986**, *83*, 1325-1329.

(9) Sauer, R. T.; Pan, J.; Hopper, P.; Hehir, K.; Brown, J.; Poteete, A. R. *Biochemistry* **1981**, *20*, 3591-3598.

(10) De Anda, J.; Poteete, A. R.; Sauer, R. T. *J. Biol. Chem.* **1983**, *258*, 10536-10542.

(11) Senn, H.; Eugster, A.; Otting, G.; Suter, F.; Wüthrich, K. *Eur. Biophys. J.*, in press.

(12) Otting, G.; Senn, H.; Wagner, G.; Wüthrich, K. *J. Magn. Reson.*, in press.

(13) Bolton, P. H. *J. Magn. Reson.* **1985**, *62*, 143-146.

[†] Present address: Pharmaceutical Division, Preclinical Research, Sandoz Ltd., CH-4002 Basel, Switzerland.